


Absence of crystals in the phase behavior of hollow microgels

A. Scotti¹, A. R. Denton², M. Brugnoli¹, R. Schweins³, and W. Richtering¹

¹*Institute of Physical Chemistry, RWTH Aachen University, 52056 Aachen, Germany*

²*Department of Physics, North Dakota State University, Fargo, North Dakota 58108-6050 USA*

³*Institut Laue-Langevin ILL DS/LSS, 71 Avenue des Martyrs, F-38000 Grenoble, France*

 (Received 26 February 2020; revised 23 July 2020; accepted 29 January 2021; published 22 February 2021)

Solutions of microgels have been widely used as model systems to gain insight into atomic condensed matter and complex fluids. We explore the thermodynamic phase behavior of hollow microgels, which are distinguished from conventional colloids by a central cavity. Small-angle neutron and x-ray scattering are used to probe hollow microgels in crowded environments. These measurements reveal an interplay among deswelling, interpenetration, and faceting and an unusual absence of crystals. Monte Carlo simulations of model systems confirm that, due to the cavity, solutions of hollow microgels more readily form a supercooled liquid than for microgels with a cross-linked core.

DOI: [10.1103/PhysRevE.103.022612](https://doi.org/10.1103/PhysRevE.103.022612)

I. INTRODUCTION

Colloidal suspensions provide important insights into phase transitions in condensed matter, e.g., crystallization and glass formation, since they offer a versatile model for studying fundamental processes in atomic systems on length and timescales accessible with conventional techniques (e.g., confocal microscopy, dynamic light scattering) [1–4]. A particular class of colloids is represented by solutions of soft, deformable microgels—polymeric cross-linked networks swollen in a good solvent that respond to external stimuli, e.g., changes in temperature [5] or pH [6]. Microgels have helped to address questions regarding the formation of soft and strong glasses [7–9] and the crystallization of spherical particles interacting via soft pair potentials [9–13], in both two [14–16] and three dimensions [17,18].

Microgels synthesized by precipitation polymerization typically comprise a dense polymeric core surrounded by a periphery (fuzzy shell) with lower polymer density (henceforth termed “regular” microgels). Improved synthesis protocols allow creating microgels with internal structures substantially different from those of regular microgels, such as hollow microgels—polymeric networks with central, solvent-filled cavities [19,20]. With no atomic counterpart, hollow microgels represent a class of materials that show unique and unexplored properties. Studies of microgels with diverse architectures have revealed that the particle “softness” depends on more than the concentration of cross-linking agent used during synthesis [21]. The central cavity allows a hollow microgel to respond to the compression of a matrix of regular microgels of comparable size and softness by rearranging its polymer chains into the cavity [22]. As a consequence, the presence of a cavity has a much stronger effect on the microgel compressibility than a significant decrease in cross-linker concentration. Indeed, the relative size change of 5 mol% cross-linked hollow microgels has been shown to be much

larger than the size change of ultralow cross-linked regular microgels [21].

In this work, we investigate the phase behavior of solutions of hollow poly(*N*-isopropylacrylamide)-based (pNIPAM) microgels as a function of concentration, cross-linker density, and cavity size. We address two main questions: (i) How do hollow microgels respond to crowding? (ii) Does the internal structure of single microgels affect colloidal phase behavior? To answer these questions, we study the phase behavior of solutions of different hollow microgels. We use hollow microgels synthesized with either 5 or 2.5 mol% cross linker and with internal cavities of different sizes. For the hollow microgels used in this study, the smaller internal cavity has a radius of 24 ± 2 nm and the larger internal cavity, present in the hollow 5 mol% cross-linked microgels, has a radius of 91 ± 4 nm.

II. SYNTHESIS

The exact synthesis of the hollow 2.5 mol% (MB-HS-60-2.5-pNIPAM) and 5 mol% cross-linked microgels (MB-HS-60-5-pNIPAM) with a sacrificial core of 60 nm has been described previously [22]. The 5 mol% cross-linked hollow microgels, deuterated (MB-HS-105-5-D7pNIPAM) and hydrogenated (MB-HS-105-5-pNIPAM), are produced by core dissolution of 105-nm silica-core pNIPAM-shell microgels [23]. The silica cores were obtained by the Stöber synthesis [24] with surface modification [25]. Briefly, 80 mL of ammonia solution was added to 700 mL of preheated ethanol. After equilibration, 24 mL of tetraethyl orthosilicate (TEOS) was added to start the reaction. Centrifugation was applied for purification and the solvent was evaporated for storage. Core-shell microgels are produced similarly to regular microgels, except for the presence of silica seeds during the polymerization. The monomer solution consists of NIPAM or D7-NIPAM, *N,N'*-methylenebisacrylamide (BIS), and sodium

TABLE I. Composition of reaction solutions during synthesis of regular and core-shell microgels and hydrodynamic radii at 20 °C and 50 °C of corresponding regular and hollow microgels. For the synthesis of the deuterated hollow microgels, D7-NIPAM ($[C_6D_7H_4NO]_n$) was used as monomer; for the hydrogenated microgels, NIPAM ($[C_6H_{11}NO]_n$) was used.

Sample name	Category	Monomer (mmol)	BIS (mmol)	SDS (mmol)	KPS (mmol)	V_{total} (mL)	$R_h^{20^\circ C}$ (nm)	$R_h^{50^\circ C}$ (nm)
MB-HS-105-5-D7pNIPAM	Hollow	9.5	0.5	0.22	0.31	200	(232±6)	(85±1)
MB-HS-105-5-pNIPAM	Hollow	9.5	0.5	0.22	0.31	200	(230±4)	(106±1)
MB-HS-60-5-pNIPAM	Hollow	10.0	0.53	0.5	0.39	250	(117±2)	(56±1)
MB-HS-60-2.5-pNIPAM	Hollow	10.2	0.26	0.5	0.39	250	(152±3)	(55±1)
MB-pNIPAM-5-225	Regular	45.0	2.37	0.04	0.47	300	(223±2)	(122±1)

dodecyl sulfate (SDS) in filtered (0.2 μ m regenerate cellulose membrane filter) double-distilled water (see Table I for exact amounts). To generate core-shell microgels, a solution of 1.4 g of the sacrificial silica cores in 3.8 mL of ethanol was added. The reaction solution was purged with nitrogen under stirring at 200 rpm and heated to 60 °C. At once, a solution of potassium peroxydisulfate (KPS) in 5 mL of water was degassed. The KPS solution was transferred into the monomer solution to initiate the reaction. The polymerization was left to proceed for 4 h at constant stirring and 60 °C. The microgels were purified by threefold centrifugation at 157 000 g and redispersion in fresh water. Lyophilization was performed for storage.

To generate the hollow microgels, the silica cores of the core-shell microgels were dissolved by means of a sodium hydroxide (NaOH) solution [23]. Finally, the resulting hollow microgels were centrifuged at 360 000 g for purification and lyophilization was carried out for storage.

III. DYNAMIC LIGHT SCATTERING

To determine the total hydrodynamic radius, R_h , the size distribution, and the swelling behavior of the hollow microgels, we used multiangle dynamic light scattering (DLS). The instrument uses a mounted laser with vacuum wavelength $\lambda_0 = 633$ nm. We studied dilute solutions of the different microgels in water, with refractive index $n(\lambda_0) = 1.33$. In the dilute regime, microgel-microgel interactions were negligible. The temperature was controlled using a thermal bath filled with toluene to match the refractive index of the glass. The scattering vector $q = (4\pi n/\lambda_0) \sin(\vartheta/2)$ was changed by varying the scattering angle, ϑ , between 30 and 130 deg, in steps of 5 deg.

Every intensity autocorrelation function acquired was analyzed with the second cumulant analysis [27]. After computing all the average decay rates, Γ , the relation, $\Gamma = D_0 q^2$, linking Γ to the scattering vector, q , was used to obtain the average diffusion coefficient, D_0 , by fitting the data of Γ versus q^2 with linear regression [28]. Finally, the Stokes-Einstein relation, $R_h = k_B T / (6\pi \eta_{H_2O} D_0)$, was used to obtain the hydrodynamic radii of the microgels in solution at different temperatures.

The values of R_h for the hydrogenated (MB-HS-105-5-pNIPAM) and deuterated (MB-HS-105-5-D7pNIPAM) 5 mol% cross-linked hollow microgels are plotted in Fig. 1(a) as

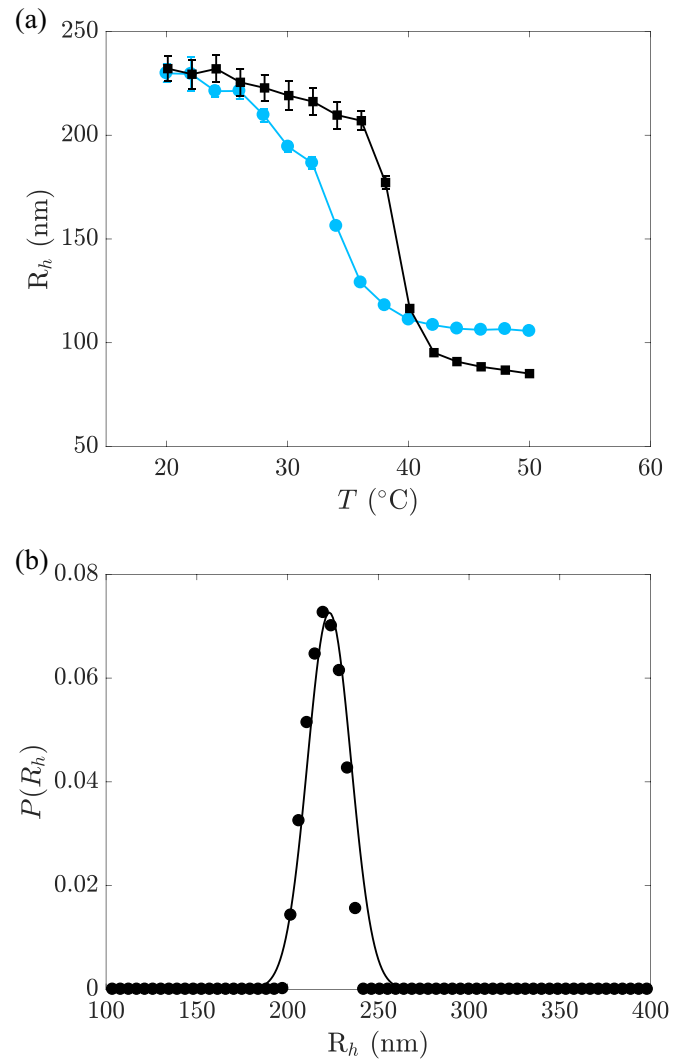


FIG. 1. (a) Hydrodynamic radius, R_h , vs temperature, T for hydrogenated (MB-HS-105-5-pNIPAM) and deuterated (MB-HS-105-5-D7pNIPAM) 5 mol% cross-linked hollow microgels used in the SAXS and SANS experiments (circles and squares, respectively). (b) Size distribution, $P(R)$, of the hydrogenated hollow 5 mol% cross-linked microgels (MB-HS-105-5-pNIPAM) at 20 °C and $\theta = 100^\circ$ as obtained from the analysis of the intensity autocorrelation function using a modified Contin algorithm (circles) [26]. The solid curve is a Gaussian fit to the data.

a function of temperature (circles and squares, respectively). As can be seen, the two types of microgel have approximately the same size at 20 °C. The deuterated 5 mol% cross-linked hollow microgels reach a smaller size at 50 °C compared with their hydrogenated counterparts. This reveals that their polymeric network is slightly softer than that of the hydrogenated 5 mol% cross-linked hollow microgels. Furthermore, as a consequence of the use of deuterated monomer during the precipitation polymerization, the volume phase transition temperature of the deuterated 5 mol% cross-linked hollow microgels is shifted to slightly higher temperature [29,30]. These effects are negligible for the aim of this study, since we work at a constant temperature of 20 °C, where the microgels used have virtually the same size and are in their swollen soft state.

The size distributions of the different microgel solutions were obtained by analyzing the intensity autocorrelation functions measured at different scattering angles using the Contin [31] algorithm modified according to Ref. [26] to have a more robust capability to choose the regularizer parameter. The values for the radii and for the size polydispersity were obtained as the mean and the standard deviation (errors) of ten measurements taken at scattering angles between 30 and 130 deg. An example of the outcome of the analysis for the hydrogenated hollow 5 mol% cross-linked microgels (MB-HS-105-5-pNIPAM in Table I) is shown in Fig. 1(b).

IV. VISCOMETRY

The thermodynamic quantity that determines the phase behavior of microgel solutions, at fixed temperature and pressure, is the generalized volume fraction, ζ [5,13], defined as the fraction of the sample volume occupied by the microgels in their fully swollen state. The capability of microgels to deform [32–34], compress [6,35], or interpenetrate each other [36,37] is reflected by values of ζ ranging above 0.74, the close-packed limit for hard spheres [38]. Note that ζ is related to the weight fraction of polymer in the solution, c , by a conversion constant k : $\zeta = kc$. Measurements of the viscosity, η , of diluted microgel solutions is the standard method to experimentally determine this constant [10,36,39], since the relative viscosity of the microgel suspension, $\eta_r = \eta/\eta_{\text{H}_2\text{O}}$, with $\eta_{\text{H}_2\text{O}}$ being the viscosity of water at 20 °C, is linked to the generalized volume fraction by the Einstein-Batchelor equation:

$$\eta_r = 1 + 2.5\zeta + 5.9\zeta^2 = 1 + 2.5kc + 5.9(kc)^2. \quad (1)$$

We prepared solutions of microgels with weight fractions in the range $5 \times 10^{-4} < c < 3 \times 10^{-3}$. For every solution, the time of fall, t , of a fixed volume of the solutions through a thin capillary of an Ubbelohde viscosimeter immersed in a water bath at 20.0 ± 0.1 °C was measured. The time of fall is linked to the kinematic viscosity, ν , by an instrumental constant, K , given by the manufacturer: $\nu = Kt$. For the instrument used for these experiments, $K = 3.156 \times 10^{-9} \text{ m}^2 \text{ s}^{-2}$. After computing the ν values for the different samples, the values of the viscosity were obtained as $\eta = \nu \rho_{\text{H}_2\text{O}}$ with $\rho_{\text{H}_2\text{O}}$ being the density of the water at 20 °C. This relation is valid under the assumption that the solution mass density is approximately equal to that of water due to the low concentration of microgels.

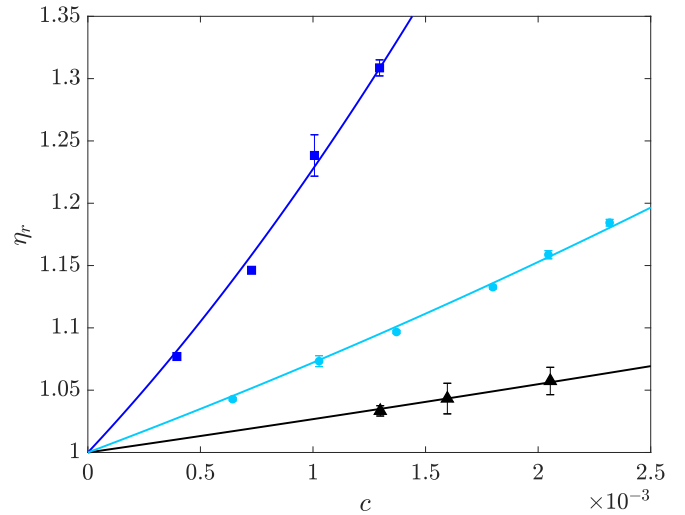


FIG. 2. Relative viscosity η_r vs polymer weight fraction c in solutions of hydrogenated hollow 5 mol% cross-linked microgels (MB-HS-105-5-pNIPAM), circles; deuterated hollow 5 mol% cross-linked microgels (MB-HS-105-5-D7pNIPAM), squares; and regular hydrogenated 5 mol% cross-linked microgels (MB-pNIPAM-5-225), triangles. Solid lines are fits of the data according to Eq. (1).

Figure 2 shows data for the relative viscosity as a function of weight fraction of microgels in solution for hydrogenated hollow, deuterated hollow, and regular 5 mol% cross-linked microgels (MB-HS-105-5-pNIPAM, MB-HS-105-5-D7pNIPAM, and MB-pNIPAM-5-225, respectively, in Table I). The conversion constants for the smaller 5 mol% cross-linked hollow microgels (MB-HS-60-5-pNIPAM in Table I) and for the 2.5 mol% cross-linked hollow microgels (MB-HS-60-2.5-pNIPAM in Table I) have been experimentally determined in Ref. [21].

V. PREPARATION OF SOLUTIONS OF HOLLOW MICROGELS

Colloidal suspensions at high concentrations are known to exhibit a supercooled liquid phase, depending on the preparation protocols. It has been reported that high levels of size-polydispersity, as well as the presence of microgels of significantly different sizes (e.g., binary mixture), dramatically slow down crystallization kinetics [13,35]. Nevertheless, within a few months from their synthesis, solutions of microgels, both binary mixtures and highly polydisperse (18.5%), reach their thermodynamic equilibrium and self-assemble into crystals at high concentrations [13]. The ability of highly polydisperse microgel solutions to form crystals has been traced to the stronger tendency of bigger microgels to deswell in a crowded environment, which decreases the polydispersity with increasing concentration [6,35]. This mechanism has been linked to the osmotic pressure of the solution determined by the counterion clouds surrounding the microgels [35,40].

All the solutions of hollow microgels presented in this study have been equilibrated for more than one and a half years. Therefore, the time allowed for the system to evolve toward equilibrium is considerably longer than in previous studies. Moreover, all the samples are hermetically sealed to

avoid problems with evaporation of the solvent. The vials containing the samples are regularly weighed to verify that solvent is not evaporated and that their packing fraction is constant. The samples are stored at constant temperature $T = 20.0 \pm 0.5^\circ\text{C}$.

Microgel assemblies in a supercooled liquid-like state can be freed from their kinetically trapped, high-energy states by thermal annealing via heating, followed by slow cooling to form well-ordered crystals. These quasistatic cooling processes, as well as gentle shearing of the samples in an oscillatory sweep, have been reported to promote crystallization of microgel solutions [10,41–44].

To guide our solutions of hollow microgels toward equilibrium, we performed heating-cooling cycles with quasistatic temperature changes ($\pm 0.2^\circ\text{C}$). The samples were first annealed by raising the sample temperature to 38°C —well above the volume phase transition temperature (VPTT)—and maintaining that temperature for time periods ranging from 1 h to 1 day. Then the samples were slowly cooled down to 20°C with a cooling rate of 0.2°C/h .

VI. PHASE BEHAVIOR OF SOLUTIONS OF HOLLOW MICROGELS

Our solutions of hollow microgels cover a range between $\zeta = 0.40 \pm 0.01$ and $\zeta = 1.05 \pm 0.02$, allowing the possibility of observing transitions from fluid to crystalline phases [5,13,45,46]. We stress that a crystalline phase has been observed for regular microgels and core-shell particles with a rigid, incompressible core surrounded by either polymers [47,48] or DNA [49,50]. Thus, the presence of a fuzzy shell *per se* does not suppress crystallization. All of the above-mentioned colloids possess a hard-sphere-like dense core. Thermodynamic phase behavior of colloidal suspensions relies on the fact that the equilibrium state minimizes the Helmholtz free energy, $F = U - TS$, where U and S are the internal energy and entropy of the system, respectively. For a suspension of hard-sphere colloids, U is independent of configuration and simply proportional to the temperature T . For certain concentrations, the entropy is maximized (i.e., F is minimized) when hard spheres self-assemble on an ordered lattice. Indeed, the loss of global configurational entropy due to collective ordering of particles is overcome by the gain in local configurational entropy deriving from the increased free volume around particles that become localized upon crystallization (see Appendix A) [51].

In contrast to colloids and microgels with a dense core, the hollow microgels studied here do not form crystals in the concentration range studied. Four different types of microgels were synthesized using either 5 or 2.5 mol% of cross linker (Table I). As mentioned above, we prepared these solutions following standard procedures to favor crystal formation, e.g., heating-cooling cycles, and letting them rest at constant T for longer than 1.5 yr.

Despite these procedures and the long time to equilibrate, none of the hollow microgel solutions studied here crystallized. Images of the series of concentrations for different solutions of hollow microgels are shown in Fig. 3. The size polydispersities p of all the microgels used in this study were determined both by fits of small-angle neutron scatter-

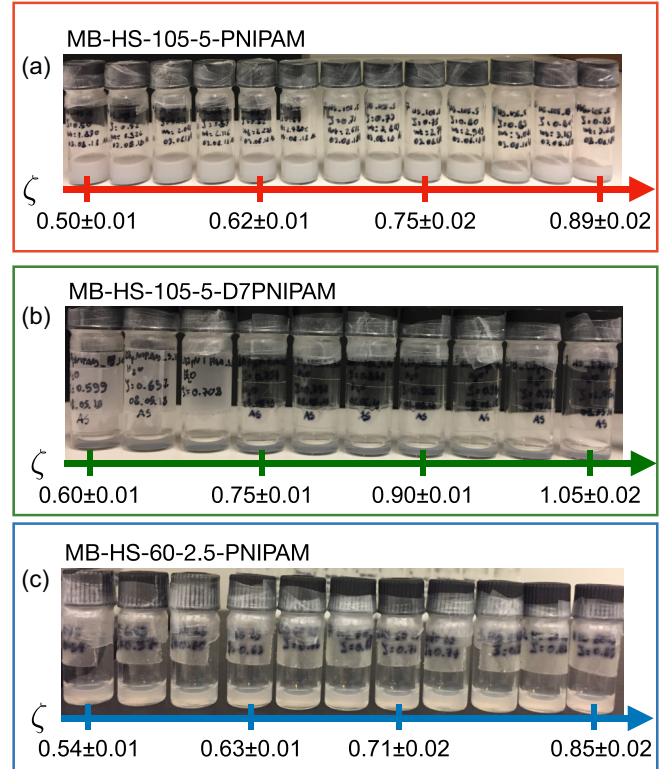


FIG. 3. Photographs of solutions of hollow microgels at different concentrations: (a) MB-HS-105-5-pNIPAM; (b) MB-HS-105-5-D7pNIPAM; (c) MB-HS-60-2.5-pNIPAM. Data relating to the synthesis and characterization of these samples are reported in Table I (and Table III in Appendix A). All samples were stored at $20.0 \pm 0.5^\circ\text{C}$. No crystals are evident up to the highest concentrations. In panels (a) and (b) the samples are contained in vials with dimensions 45×14.75 mm, while in panel (c) the samples are contained in vials with dimensions 32×11.6 mm.

ing data of dilute solutions of hollow microgels [21,22,52] and by analysis of dynamic light scattering autocorrelation functions with a custom-written Contin algorithm [26], which yields the microgel size distribution (see Fig. 1). As seen in Appendix A (Table III), at least two of the hollow microgel samples have $p \ll 10\%$, well below the threshold for suppressing crystallization, not only for regular microgels but also for hard spheres [13,53].

Furthermore, the capability of microgels to spontaneously deswell [6,35,53] significantly decreases the size polydispersity that suppresses the liquid-to-solid transition for hard spheres. Consequently, crystals can form well above the polydispersity limit known for hard-sphere fluids ($p = 12\%$) [38], as is the case for the regular microgels with outer radius 209 ± 4 nm and $p = 13.2 \pm 0.9\%$ (Fig. 4). Therefore, polydispersity *per se* cannot explain the absence of crystals in the phase behavior of hollow microgels.

VII. SMALL ANGLE X-RAY SCATTERING FROM CONCENTRATED SOLUTIONS

To verify whether crystals were forming in the solutions but were not visible to the naked eye, we measured all our

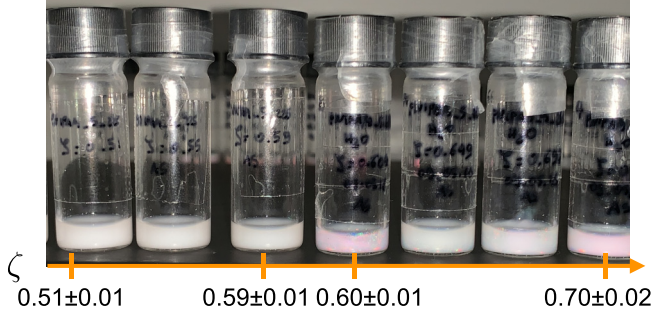


FIG. 4. Photographs of solutions of regular hydrogenated 5 mol% cross-linked microgels (MB-pNIPAM-5-225 in Table I) at different generalized volume fractions ζ . Crystals are visible, from Bragg diffraction, for $0.59 \pm 0.01 < \zeta < 0.70 \pm 0.02$. Samples are contained in vials with dimensions 45×14.75 mm and stored at $T = 20.0 \pm 0.5$ °C.

solutions using small-angle x-ray scattering (SAXS). In these experiments, the intensity, $I(q)$, is measured as a function of the scattering vector $q = (4\pi/\lambda) \sin(\theta/2)$, with λ and θ being the radiation wavelength and the scattering angle, respectively. For concentrated solutions of microgels, $I(q)$ is directly proportional to the form factor, $P(q)$, and the structure factor, $S(q)$. The form factor and structure factor contain information about the characteristic length scales of, respectively, a single microgel and an assembly of microgels. If crystals are present in solution, distinctive Bragg peaks are clearly visible in $I(q)$. From the peak positions, it is possible to uniquely identify the crystalline lattice formed [13,39,54].

The measurements for this study have been performed at the Swiss Light Source, Paul Scherrer Institut (Villigen, Switzerland), using the cSAXS instrument. The x-ray wavelength was set to $\lambda = 0.143$ nm with an error of 0.02% over λ resolution. The detector was positioned at a distance of 7.12 m from the sample. The collimated beam illuminated an area of about 200×200 μm . The instrument mounts a two-dimensional (2D) detector with a pixel size of 172×172 μm^2 and 1475×1679 pixels.

The SAXS intensities in Fig. 5 are relative to hollow 5 mol% cross-linked microgels with outer radius 210 ± 8 nm and internal cavity radius 91 ± 4 nm (MB-HS-105-5-pNIPAM in Table I). The absence of Bragg peaks indicates a disordered arrangement of microgels [13,54].

A. Structure factors from concentrated solutions

The structure factors, $S(q)$, shown in Fig. 6 are a few examples of those obtained by dividing the scattered intensity of solutions of hydrogenated hollow 5 mol% cross-linked microgels (MB-HS-105-5-pNIPAM in Table I), $I(q)$, by the form factor measured in a dilute solution of the same microgels at $\zeta = 0.08 \pm 0.01$. In this way, we neglected the variation of the form factor of the microgels due to the increase of ζ [13,35,36,39,55]. Nevertheless, it has been shown that this approximation leads to an error in the position of the first peak in $S(q)$ of only $\approx 2\%$ [13,39]. The thick curves represent Gaussian fits of the first peak. From the position of the first peak, $q_{1,\text{peak}}$, we can obtain the nearest neighbor distance, $d_{nn} \simeq 2\pi/q_{1,\text{peak}}$ [36,56]. The shift of the first peak of the

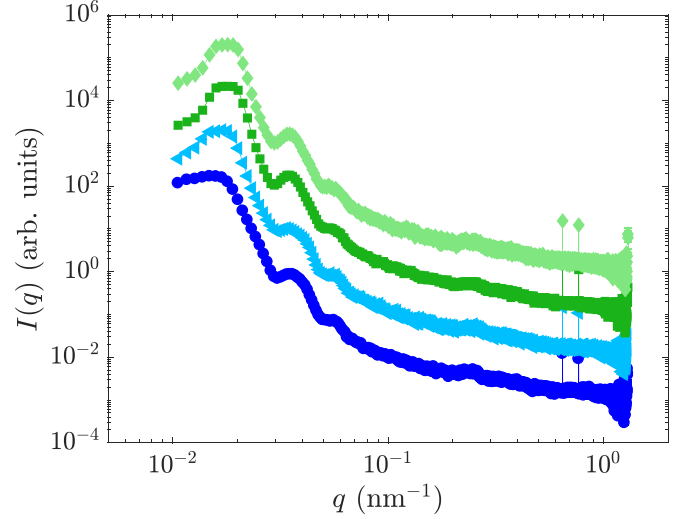


FIG. 5. SAXS intensities, $I(q)$, vs scattering vector, q , of solutions of hollow 5 mol% cross-linked microgels with outer radius 210 ± 8 nm and internal cavity radius 91 ± 4 nm (MB-HS-105-5-pNIPAM in Table I). Concentrations: $\zeta = 0.60 \pm 0.01$ (circles), $\zeta = 0.75 \pm 0.02$ (triangles), $\zeta = 0.85 \pm 0.02$ (squares), and $\zeta = 0.90 \pm 0.02$ (diamonds). All measurements were made at $T = 20$ °C.

structure factor to higher q values with increasing ζ reflects a decrease of the microgel center-to-center separation. As already observed for the $I(q)$ in Fig. 5, the absence of sharp Bragg peaks indicates that crystals are absent in these solutions. To gain complementary information on the response of individual hydrogenated hollow 5 mol% cross-linked microgels (MB-HS-105-5-pNIPAM), we performed small-angle neutron scattering experiments.

VIII. SMALL-ANGLE NEUTRON SCATTERING WITH CONTRAST VARIATION

To probe the response of these hollow 5 mol% cross-linked microgels in crowded environments, we used small-angle neutron scattering (SANS) with contrast variation [22,35,36,55]. In contrast to x rays, which interact electromagnetically with the electronic clouds surrounding the atoms, neutrons interact with the nuclei via the strong nuclear force. The practical consequence of this difference is that the scattering, in particular, the contrast (scattering length), varies systematically along the periodic table, allowing us to distinguish both atoms with similar atomic numbers and isotopes of the same element. For the study presented here, the difference in scattering length between hydrogen and deuterium is of fundamental importance [57]. Indeed, by means of selective deuteration of the monomer used in the synthesis of the microgels, and using the proper mixture of water and heavy water, it is possible to contrast match part of the sample. Here we used relatively few hollow microgels made of pNIPAM ($[\text{C}_6\text{H}_{11}\text{NO}]_n$) dispersed in a matrix of 5 mol% cross-linked D7-pNIPAM-based hollow microgels ($[\text{C}_6\text{D}_7\text{H}_4\text{NO}]_n$) of comparable size (see Fig. 19 of Appendix B and Table III of Appendix C). The solvent is a mixture of water and heavy water matching the neutron scattering length density of the deuterated microgels [21,22,35,36,54]. Consequently, the majority of microgels

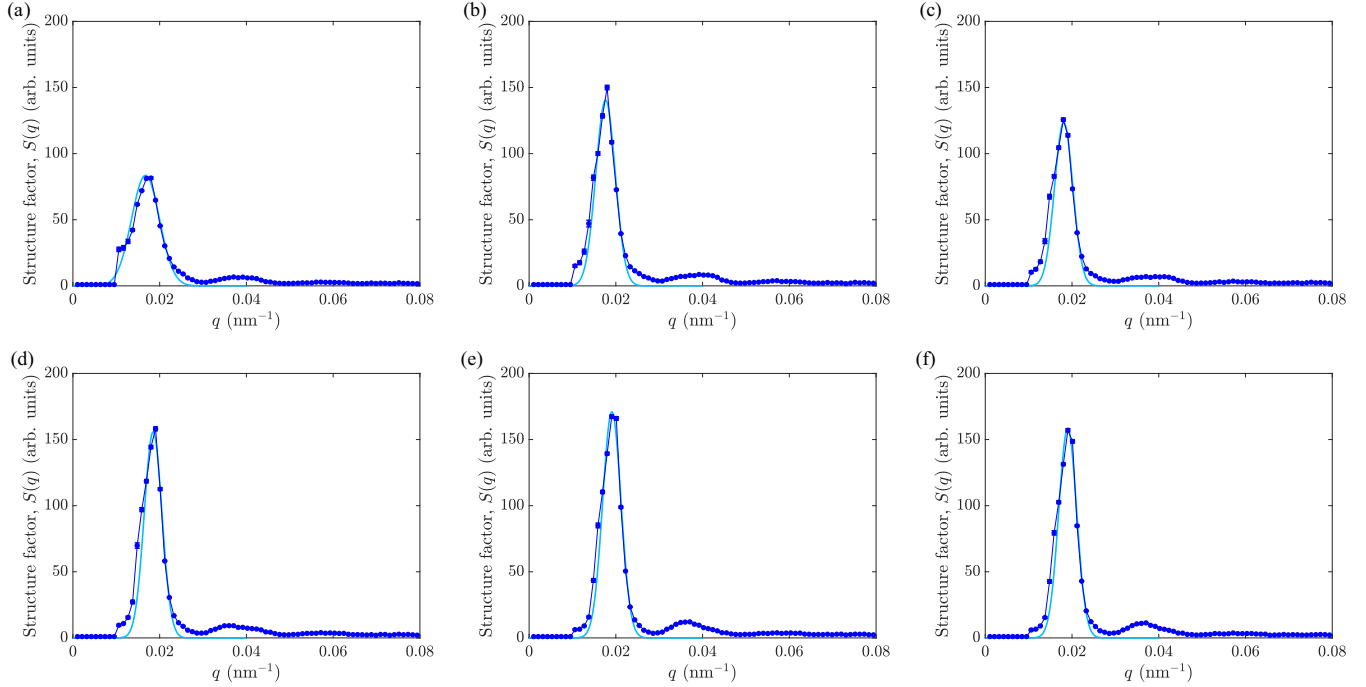


FIG. 6. Structure factors, $S(q) = I(q)/I(q, \zeta = 0.08)$, vs scattering vector, q , of solutions of the hydrogenated hollow 5 mol% cross-linked microgels in Fig. 3(a) measured with SAXS at different concentrations (blue circles): $\zeta = 0.60 \pm 0.01$ (a), 0.70 ± 0.01 (b), 0.75 ± 0.02 (c), 0.80 ± 0.02 (d), 0.85 ± 0.02 (e), and 0.95 ± 0.02 (f). Light blue solid lines: Gaussian fits of the first peak of the structure factors.

in solution are invisible, i.e., $S(q) = 1$. Therefore, in these measurements, we directly probe the form factor of the few hydrogenated hollow 5 mol% cross-linked microgels, and we can monitor its changes as a function of concentration [21,22,35,36,39,54].

The SANS measurements were performed on the D11 small-angle neutron scattering instrument at the Institut Laue-Langevin (ILL), Grenoble, France. Three configurations were used to cover the q range of interest: sample-detector distance $d_{SD} = 34, 8$, and 2 m, all with wavelength $\lambda = 0.6$ nm. Data were corrected by subtracting the dark count and background.

The generalized volume fraction of the hydrogenated hollow 5 mol% cross-linked microgels is kept constant at $\zeta_H = 0.080 \pm 0.003$ in all SANS measurements. In contrast, for the matrix of hollow deuterated microgels, ζ_D ranges between 0 and 1.11 ± 0.03 . Therefore, $\zeta = \zeta_H + \zeta_D$ spans minimum and maximum values of 0.08 and 1.19, respectively.

A. Form factor model: Fuzzy-shell core model

The fuzzy-shell core model was used to fit the scattering data of the hollow microgels [58]. In the following, the characteristic length scales for the model can be seen in the sketch of Fig. 7. The model describes a fuzzy-shell core model with an interpenetrating layer of core and shell of thickness $2\sigma_{int}$ and a fuzzy outer surface with an extension σ_{ext} . The widths of the core and shell boxes are labeled as w_{core} and w_{shell} . The scattering amplitude of a core-shell particle $A(q)$ is expressed as

$$A(q) = \Delta\rho_{shell}V_{shell}\Phi_s(q, R_{ext}, \sigma_{ext}) + (\Delta\rho_{core} - \Delta\rho_{shell})V_{core}\Phi_{core}(q, R_{int}, \sigma_{int}), \quad (2)$$

where $\Delta\rho$ is the difference between the scattering length density of the solvent and the core (or the shell) and V_{core} and V_{shell} are the volumes of the core and the shell, respectively. The radii are defined as $R_{int} = w_{core} + \sigma_{int}$ and $R_{ext} = w_{core} + 2\sigma_{int} + w_{shell} + \sigma_{ext}$, while $\Phi(q, R, \sigma)$ represents the normalized Fourier transform of the radial density profile

$$\Phi(q, R, \sigma) = \frac{1}{V_n} \left[\left(\frac{R}{\sigma^2} + \frac{1}{\sigma} \right) \frac{\cos[q(R + \sigma)]}{q^4} + \left(\frac{R}{\sigma^2} - \frac{1}{\sigma} \right) \frac{\cos[q(R - \sigma)]}{q^4} - \frac{3 \sin[q(R - \sigma)]}{q^5 \sigma^2} - \frac{2R \cos(qR)}{q^4 \sigma^2} + \frac{6 \sin(qR)}{q^5 \sigma^2} \right], \quad (3)$$

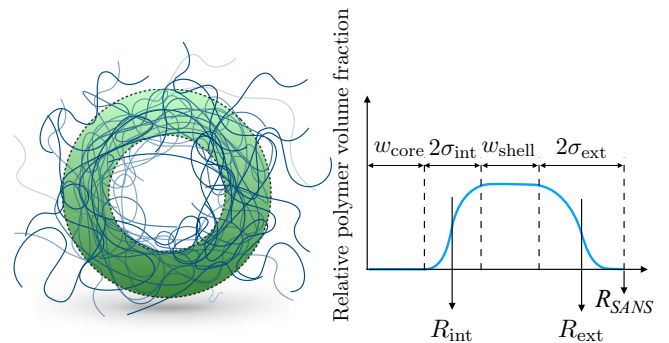


FIG. 7. Sketch of a hollow microgel and of the relative polymer volume fraction density profile with the corresponding characteristic length scales.

with $V_n = R^3/3 + R\sigma^2/6$ and q is the scattering vector [58,59]. Finally, the form factor, $P(q)$, is proportional to the scattering length amplitude squared:

$$P(q) \propto A^2(q). \quad (4)$$

In the literature, it is common to express $R_{\text{SANS}} = w_{\text{core}} + 2\sigma_{\text{int}} + w_{\text{shell}} + 2\sigma_{\text{ext}}$ to account for the polymer dangling chains in the microgel periphery [35,45,58,60]. The size polydispersity is accounted for by convolution of the form factor with a Gaussian of width $2\sigma_{\text{poly}}$. The size polydispersity is usually expressed as $p = 2\sigma_{\text{poly}}/R_{\text{SANS}}$. The scattering at high q values resulting from inhomogeneities in the polymer network due to the cross linking are accounted for by a Lorentzian term, which is added to the fitting models: $I_{\text{chain}}(0)/(1 + q^2\xi^2)$, with $I_{\text{chain}}(0)$ being the value of the scattered intensity due to the chain at $q = 0$ and ξ being the average mesh size of the polymeric network [5,61]. A constant background is added to account for the incoherent scattering. Finally, the model is convoluted with a resolution function to account for the smearing due to the instrument [62]. We considered the instrument resolution due to the velocity selector, $\Delta\lambda/\lambda = 9\%$, and the fact that the instrument is equipped with a ^3He detector with a pixel size = 7.5 mm. This model is used to fit all the SANS data reported in this work.

B. Hydrogenated hollow 5 mol% cross-linked microgels in a matrix of deuterated hollow 5 mol% cross-linked microgels

Figure 8(a) shows the measured form factors of the hydrogenated hollow 5 mol% cross-linked microgels at different ζ at 20 °C. The data are fitted (solid lines) with the fuzzy-shell core model described above and previously used to fit SANS data obtained from similar systems [20–22,52]. From the fits, the radial profiles of the relative polymer volume fraction within the microgels are obtained and plotted in Fig. 8(b) (and Fig. 21 in Appendix E).

Below the VPTT, the radial profile of the hydrogenated hollow 5 mol% cross-linked microgels (circles) shows an internal cavity of radius 91 ± 4 nm. The hollow microgels display fuzziness toward both the cavity and the outer periphery. Between these two regions, we observe a region of constant polymer concentration. The outer radius of the microgels is $R_{\text{SANS}} = 210 \pm 8$ nm with $p = 14 \pm 1\%$. The fit of static light scattering intensity confirms the radial profile obtained from the SANS data (see Fig. 20 of Appendix D). The cavity is maintained even above the VPTT (see Fig. 21 of Appendix E), as expected [20,22,23,52,59].

Figure 8(b) shows that at $\zeta = 0.30 \pm 0.01$ the radial profile of the hydrogenated hollow 5 mol% cross-linked microgels (left-side triangles) virtually coincides with the radial profile at $\zeta = 0.080 \pm 0.003$ (circles). The outer radius is 204 ± 5 nm, $p = 13.7 \pm 0.9\%$, and the internal cavity radius is 91 ± 2 nm.

At $\zeta = 0.65 \pm 0.01$, the radial profile of the hydrogenated hollow 5 mol% cross-linked microgels (squares) shows a decrease of the external fuzziness and partial occupation of the cavity by the polymer. From the fit, we obtain $R_{\text{SANS}} = 190 \pm 8$ nm, $p = 14 \pm 1\%$, and a cavity radius of 80 ± 2 nm.

At $\zeta = 0.87 \pm 0.02$ (diamonds), well above the limit where hard spheres make contact in a random close-packed

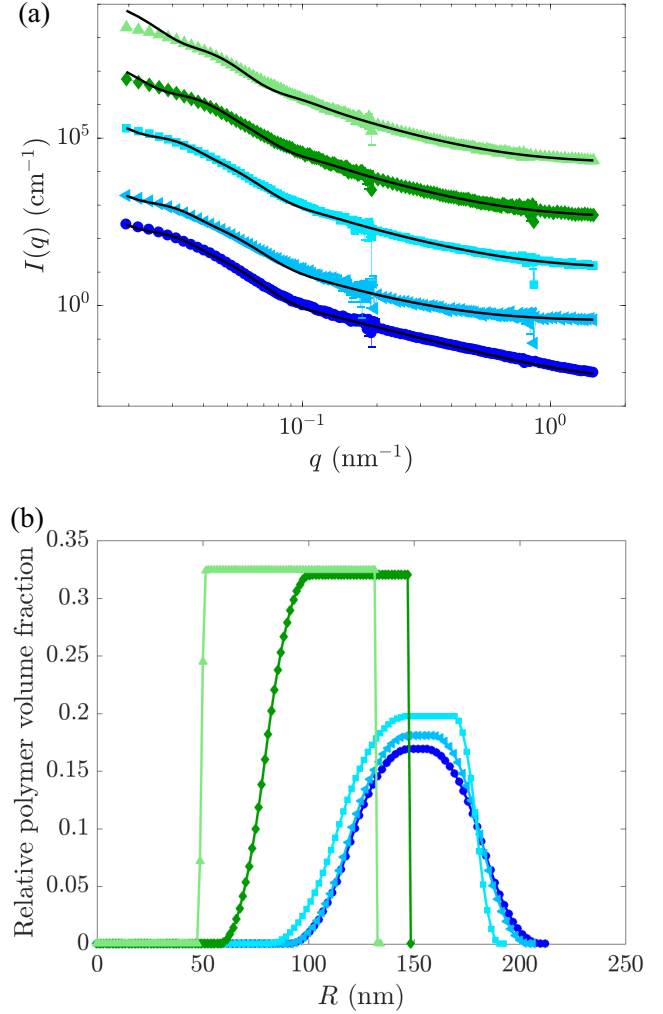


FIG. 8. (a) SANS intensities, $I(q)$, vs scattering vector, q , of hydrogenated hollow 5 mol% cross-linked microgels (MB-HS-105-5-pNIPAM in Table I). (b) Radial distribution of relative polymer volume fraction obtained by fitting curves in (a) using model of Ref. [23]. Concentrations: $\zeta = 0.080 \pm 0.003$ (circles), 0.30 ± 0.01 (left-side triangles), 0.65 ± 0.01 (squares), 0.87 ± 0.02 (diamonds), 1.19 ± 0.03 (upside triangles). All measurements were made at $T = 20$ °C. Colors, symbols, and concentrations in panel (b) correspond to those in panel (a).

state ($\zeta_{\text{rep}} = 0.64$), a significant compression is observed: $R_{\text{SANS}} = 147 \pm 6$ nm. The external fuzziness disappears and the internal cavity radius decreases to 58 ± 3 nm. At the highest concentration measured, $\zeta = 1.19 \pm 0.03$ (upside triangles), the outer radius further decreases to $R_{\text{SANS}} = 133 \pm 5$ and the cavity radius equals 47 ± 2 nm. Notably, the cavity is preserved throughout the entire ζ range probed (Fig. 21).

C. Hydrogenated regular 5 mol% cross-linked microgels in a matrix of deuterated hollow 5 mol% cross-linked microgels

As a comparison to the deswelling of hydrogenated hollow 5 mol% cross-linked microgels embedded in a matrix of deuterated hollow 5 mol% cross-linked microgels, we used SANS to measure the response of a few hydrogenated regular 5 mol% cross-linked microgels embedded in the very same

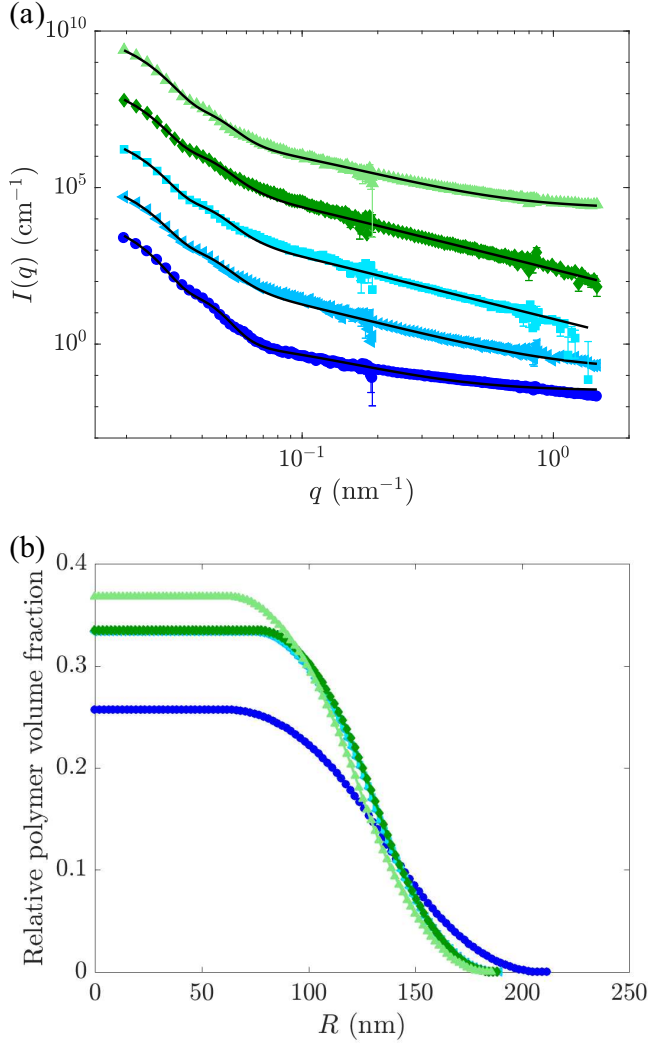


FIG. 9. (a) SANS intensities, $I(q)$, vs scattering vector, q , of hydrogenated regular 5 mol% cross-linked microgels. (b) Radial distribution of relative polymer volume fraction obtained by fitting curves in panel (a) using model of Ref. [60]. Concentrations: $\zeta = 0.080 \pm 0.003$ (circles), 0.30 ± 0.01 (left-side triangles), 0.65 ± 0.02 (squares), 0.87 ± 0.02 (diamonds), 1.19 ± 0.03 (upside triangles). All measurements were made at $T = 20^\circ\text{C}$. Colors, symbols, and concentrations in panel (b) correspond to those in panel (a).

matrix of deuterated hollow 5 mol% cross-linked microgels as before. All the microgels used have comparable swollen sizes (≈ 210 nm), as listed in Table I. Furthermore, the same amount of cross-linking agent was used to synthesize all the microgels used for the SANS experiments, i.e., all the polymeric networks have a comparable number of cross links and therefore softness.

The results of these experiments, SANS scattered intensities versus scattering vector, are plotted in Fig. 9(a) and fitted using the model for a fuzzy polydisperse sphere [60] to obtain the characteristic lengths of the regular microgels. As seen in Fig. 9(b), the radial distributions of the hydrogenated 5 mol% cross-linked microgels change only slightly with increasing ζ , revealing that once they are embedded in the very same matrix as their hollow counterpart, at the very same concentrations,

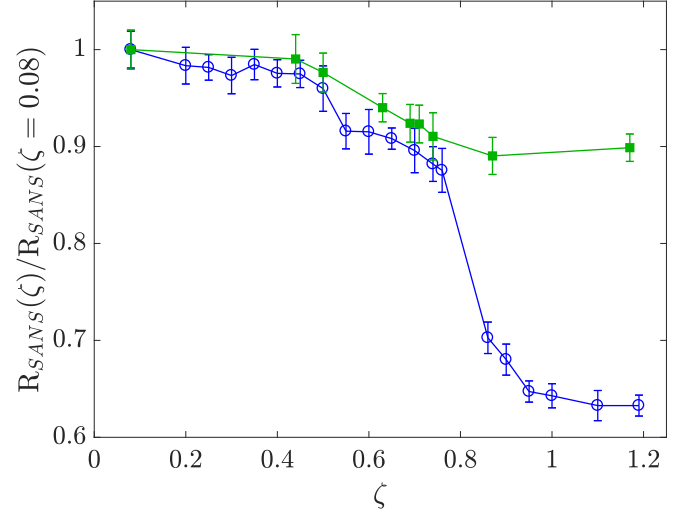


FIG. 10. Variation of the radius measured with SANS divided by the radius at $\zeta = 0.080 \pm 0.003$ and $T = 20.0 \pm 0.01^\circ\text{C}$ vs the generalized volume fraction, ζ , for hydrogenated hollow 5 mol% cross-linked microgels (empty circles) and hydrogenated regular 5 mol% cross-linked microgels (solid squares).

the regular microgels retain more their shape and structure, i.e., they are less compressible than hollow microgels.

In Fig. 10, the values of total size of the hydrogenated regular 5 mol% cross-linked microgels, R_{SANS} , divided by the radius at $\zeta = 0.080 \pm 0.003$ and $T = 20.0 \pm 0.01^\circ\text{C}$ (solid squares) are compared to the corresponding values obtained for the hydrogenated hollow 5 mol% cross-linked microgels (empty circles). The hydrogenated hollow 5 mol% cross-linked microgels embedded in a matrix of deuterated hollow 5 mol% cross-linked microgels collapse, at $\zeta = 1.19 \pm 0.03$, to a size that is $\approx 63\%$ of their fully swollen size (Fig. 10). In contrast, regular hydrogenated 5 mol% cross-linked microgels embedded in the very same matrix of deuterated hollow 5 mol% cross-linked microgels deswell to a size that is, at $\zeta = 1.17 \pm 0.03$, only 90% of the fully swollen size (Figs. 9 and 10), implying that regular microgels synthesized with the very same amount of cross-linker agents are much less compressible than hollow microgels. The presence of a dense core limits the rearrangement of polymeric chains inside the microgels, while hindering interpenetration.

D. Faceting of hollow microgels at high concentrations

We notice that for the hydrogenated hollow 5 mol% cross-linked microgels embedded in the matrix of deuterated hollow 5 mol% cross-linked microgels the size polydispersity increases with increasing ζ and reaches $p = 21 \pm 2\%$ for $\zeta = 1.10 \pm 0.02$ (Fig. 11). This trend can be explained by the faceting observed for microgels with increasing ζ [8,22,37]. Indeed, in our simple form factor model of spherical microgels, the only way to account for deformation or faceting results in an increase of the polydispersity fitting parameter, now seen as an apparent polydispersity, which reflects deformations. An increase of the apparent polydispersity has been observed both for nanoemulsion droplets [63] and in solutions of ultralow cross-linked microgels [39] and explained by the

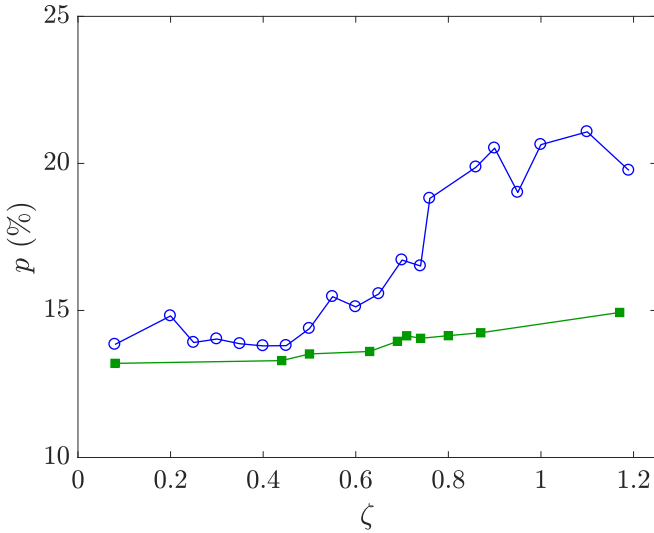


FIG. 11. Apparent size polydispersity, p , vs generalized volume fraction, ζ , for the hydrogenated hollow 5 mol% cross-linked microgels (circles) and hydrogenated regular 5 mol% cross-linked microgels (squares) embedded in the very same matrix of deuterated hollow 5 mol% cross-linked microgels.

faceting of these soft objects. As a comparison, in Fig. 11 we plot the trend of the apparent polydispersity, p , in the case of regular 5 mol% cross-linked microgels embedded in the very same matrix of hollow deuterated 5 mol% cross-linked microgels used in the previous experiments (solid squares). The parameter p only slightly increases from $13.2 \pm 0.9\%$ at $\zeta = 0.080 \pm 0.003$ to $17 \pm 1\%$ at $\zeta = 1.17 \pm 0.03$. This indicates that the regular microgels present less faceting with respect to the hollow microgels once they are embedded in the very same environment.

E. Anisotropic deformation of hollow microgels

To check whether the deformation of the hollow microgels is anisotropic, especially at high packing fractions, we tried to fit the data using a model for a hollow spheroid (i.e., an ellipsoid with $R_x = R_y \neq R_z$). We define the radius in the x - y plane (equatorial plane) $R_x = R_y = R_{\text{tot, eq}}$ and the radius in the z direction (polar plane) $R_z = R_{\text{tot, pol}}$.

This model for an empty ellipsoidal shell has as parameters the radius of the cavity of the ellipsoid in the x - y plane, R_{eq} , and the thickness of the shell (without fuzziness) in the x - y plane, D_{eq} . The total principal axis of the ellipsoid in the x - y plane is $R_{\text{tot, eq}} = R_{\text{eq}} + D_{\text{eq}}$. Additional parameters of the fit are the ratios $l = R_{\text{pol}}/R_{\text{eq}}$ and $L = D_{\text{pol}}/D_{\text{eq}}$, where R_{pol} and D_{eq} are the radius of the cavity and the thickness of the shell (without fuzziness) in the z plane, respectively. From the values of these fitting parameters, the polar radius of the cavity of the ellipsoid, $R_{\text{pol}} = lR_{\text{eq}}$, and the shell thickness (without fuzziness) in the z plane, $D_{\text{pol}} = LD_{\text{eq}}$, can be computed. The total polar principal axis of the ellipsoid is $R_{\text{tot, pol}} = R_{\text{pol}} + D_{\text{pol}}$. The model used is implemented within SASVIEW 4.2.2 software. As for the spherical models, a Lorentzian term, to account for the inhomogeneities of the polymeric network, and a constant background were added to the ellipsoidal model to correctly reproduce the data at high q .

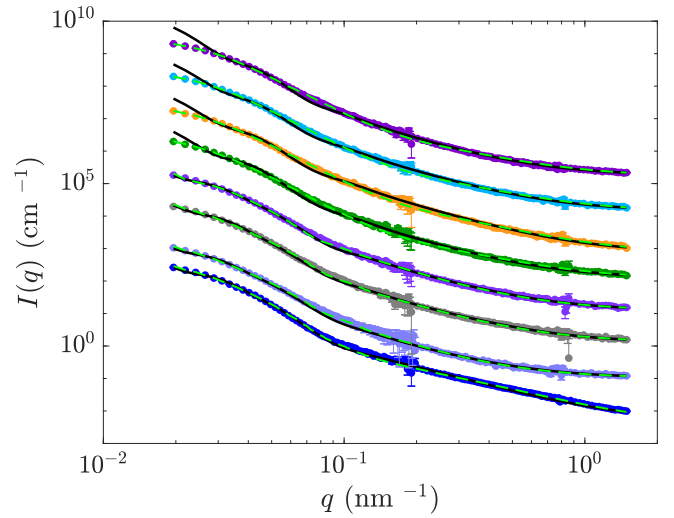


FIG. 12. SANS intensities, $I(q)$, vs scattering vector, q , of hydrogenated hollow 5 mol% cross-linked microgels with $\zeta_H = 0.080 \pm 0.003$ measured with contrast variation for concentrations, from bottom to top: $\zeta = 0.080 \pm 0.003$, 0.50 ± 0.01 , 0.65 ± 0.01 , 0.74 ± 0.01 , 0.90 ± 0.02 , 1.00 ± 0.02 , 1.10 ± 0.02 , and 1.19 ± 0.03 . The solid lines represent fits with the hollow fuzzy-sphere model, while the dashed lines represent fits of the data with the ellipsoidal model.

Figure 12 shows as an example the SANS intensities, $I(q)$, of the hydrogenated hollow 5 mol% cross-linked microgels with $\zeta_H = 0.080 \pm 0.003$ measured with contrast variation for concentrations, from bottom to top: $\zeta = 0.080 \pm 0.003$, 0.50 ± 0.01 , 0.65 ± 0.01 , 0.74 ± 0.01 , 0.90 ± 0.02 , 1.00 ± 0.02 , 1.10 ± 0.02 , and 1.19 ± 0.03 . The solid lines represent the fit of the data using the hollow fuzzy-sphere model, while the dashed curves are fits of the same data using the ellipsoidal model.

As can be seen, the fits with the two models virtually coincide for concentrations $\zeta < 0.8$. For these samples, the fitting parameters that describe the anisotropy of the microgels, l and L , are ≈ 1 , indicating that there is not a significant shape deformation (Table II). We have $R_{\text{eq}} = R_{\text{pol}} \approx R_{\text{SANS}}$ and also the size of the internal cavity is consistent with the values determined by SANS. The differences in the characteristic sizes of the microgels determined by the two models can be understood since, for simplicity and to limit the number of fitting parameters, the ellipsoidal model does not account for internal or external fuzziness of the microgels. This limitation of the model might explain the differences in values of the shell thickness or cavity radius. Nevertheless, for $\zeta \lesssim 0.75$ no significant anisotropy can be detected and therefore the increase of the value of the fitting parameter describing the apparent polydispersity is mainly due to the faceting of the microgels, which cannot be resolved within the SANS resolution. We note that the fact that microgels in crowded environments first facet and then isotropically collapse is in agreement both with direct imaging reported by de Aguiar *et al.* (confocal) [32] and by Conley *et al.* (super resolution) [37] and with observations based on measurements of the suspension osmotic pressure [34].

For concentrations $\zeta \geq 0.90 \pm 0.02$, the dashed lines describe more accurately the SANS intensities, especially for

TABLE II. Generalized packing fraction, ζ , and characteristic lengths for the spherical and ellipsoidal fits of the SANS data in Fig. 12.

ζ	Sphere			Ellipsoid				
	R_{SANS} (nm)	w_{core} (nm)	R_{eq} (nm)	l	D_{eq} (nm)	L	R_{pol} (nm)	D_{pol} (nm)
0.080 ± 0.003	210 ± 8	91 ± 4	135 ± 10	1.00 ± 0.01	90 ± 3	1.00 ± 0.01	135 ± 11	90 ± 4
0.50 ± 0.01	201 ± 7	96 ± 3	129 ± 8	1.01 ± 0.01	88 ± 3	1.00 ± 0.01	130 ± 9	87 ± 4
0.65 ± 0.01	190 ± 8	81 ± 5	120 ± 8	1.05 ± 0.01	88 ± 2	1.02 ± 0.01	126 ± 10	90 ± 3
0.74 ± 0.01	185 ± 7	99 ± 3	105 ± 7	1.02 ± 0.03	89 ± 4	1.04 ± 0.03	107 ± 10	93 ± 7
0.90 ± 0.02	143 ± 5	49 ± 3	30 ± 4	0.79 ± 0.02	87 ± 3	0.35 ± 0.02	24 ± 4	30 ± 3
1.00 ± 0.02	135 ± 6	55 ± 3	31 ± 4	0.91 ± 0.03	76 ± 2	0.35 ± 0.03	29 ± 5	26 ± 3
1.10 ± 0.02	133 ± 7	51 ± 4	29 ± 3	0.98 ± 0.03	77 ± 5	0.35 ± 0.01	28 ± 4	27 ± 3
1.19 ± 0.03	133 ± 5	47 ± 2	30 ± 4	0.90 ± 0.05	69 ± 4	0.32 ± 0.03	26 ± 5	22 ± 3

very low values of q . For these fits, the parameters reflecting the anisotropy of the microgels are smaller than one: $0.8 \lesssim l \lesssim 0.95$ and $0.3 \lesssim L \lesssim 0.35$ (Table II). This result indicates that, well above random close packing, the microgels become oblate spheroids ($R_{\text{eq}} > R_{\text{pol}}$). Furthermore, it seems that the cavity maintains a more spherical shape, $l \simeq 1$, while the shell becomes more anisotropic $L \ll 1$.

Even in this case, however, we have to take care not to overinterpret the data. Since the simple model we are using for the ellipsoidal particles does not account for both fuzziness and faceting, it might be that such a strong decrease of the parameter L is a consequence of faceting. Acknowledging this possibility, we can still see that, at very high packing fractions, the microgels are better described by an anisotropic object and, therefore, it is reasonable to consider this effect being present, most likely at the same time with faceting.

IX. COMPARISON BETWEEN SMALL-ANGLE X-RAY AND NEUTRON SCATTERING RESULTS

Figure 13 summarizes how the outer diameter of the hydrogenated hollow 5 mol% cross-linked microgels, $2R_{\text{SANS}}$, varies with ζ (empty circles). Four regimes can be identified: (i) for $\zeta < 0.50 \pm 0.01$, the hydrogenated hollow 5 mol% cross-linked microgels maintain their size; (ii) for $0.50 \pm 0.01 < \zeta < 0.76 \pm 0.01$, the size first decreases; (iii) for $0.76 \pm 0.02 < \zeta < 1.10 \pm 0.3$, the size further steeply decreases; and (iv) for $\zeta > 1.10 \pm 0.02$, the size remains constant.

The onset of deswelling in regime (ii) occurs at concentrations below that at which the microgels make contact. This phenomenon has been reported also for regular microgels [6,13,22,53] and attributed to overlapping of counterion clouds surrounding the microgels, significantly increasing the osmotic pressure of the solution [35,40]. In contrast, the second stage of deswelling in regime (iii) is due to a collapse of the external fuzzy shell and rearrangement of polymer within the cavity.

To understand whether microgel deswelling is sufficient to forestall interpenetration, the diameter of the hollow microgels obtained by SANS is compared to the nearest neighbor distance, d_{nn} (solid circles in Fig. 13). The latter is obtained from the structure factor (Fig. 6) of the solutions shown in Fig. 3(a), measured with SAXS. The red curve in Fig. 13 represents a fit of the data with the power law $d_{nn} = c\zeta^{-1/3}$, c being the value of d_{nn} at $\zeta = 1$. This curve divides the graph

into two regions, shaded as yellow and green areas. If the microgels have diameters (empty circles) above the red curve, in the yellow area, their size exceeds the nearest-neighbor distance between microgels and, therefore, interpenetration or faceting is dominant. In contrast, if the diameter lies below the red curve, in the green area, then the microgels are smaller than the nearest neighbor distance. In this case, interpenetration and faceting are negligible and the microgels are instead deswollen or deformed.

For $0.5 \lesssim \zeta \lesssim 0.8$, the empty circles in Fig. 13 lie in the yellow area, indicating interpenetration or faceting of the hollow microgels with their neighbors. In contrast, for $\zeta \gtrsim 0.8$, $2R_{\text{SANS}}$ is consistently smaller than d_{nn} , indicating stronger deswelling or deformation and negligible interpenetration or faceting.

This deswelling behavior can be explained by the absence of a polymeric core, making the hollow microgels more compressible and interpenetrable than regular microgels with a dense core surrounded by a fuzzy shell. Furthermore, as

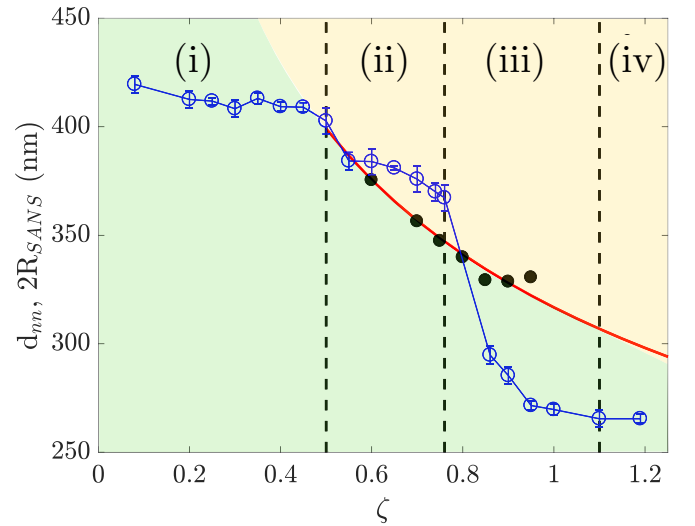


FIG. 13. Particle diameter $2R_{\text{SANS}}$ (measured with SANS, empty circles) and nearest neighbor distance d_{nn} (measured with SAXS, solid circles) vs generalized volume fraction ζ for hollow microgel solutions. Red curve is a fit of the d_{nn} data to the function $c\zeta^{-1/3}$ with fit parameter c . The vertical dashed lines mark the border of the different compression regimes (i) to (iv).

reported above, faceting and anisotropic deformations play a role for the higher concentrations.

X. COMPUTER SIMULATIONS

To complement our experiments, test our interpretations, and independently evaluate the effect of cavities on equilibrium thermodynamic properties and phase behavior of hollow microgel solutions, we performed Monte Carlo (MC) simulations of model systems.

A. Flory-Hertz model of hollow microgels

We consider N hollow microgels dispersed in a solvent. Each microgel, consisting of N_{mon} monomers and N_{ch} cross-linked chains, has in its collapsed state an inner (cavity) radius a_0 and outer radius b_0 , and in its swollen state an inner radius a and outer radius b . For simplicity, we assume the cross links to be uniformly distributed throughout the shell volume. Under the assumption that monomers in the collapsed state are randomly close packed with volume fraction 0.63, the monomer numbers are related to the collapsed radii according to

$$N_{\text{mon}} = 0.63 \frac{b_0^3 - a_0^3}{r_{\text{mon}}^3}, \quad (5)$$

where $r_{\text{mon}} \simeq 0.3$ nm is a typical monomer radius. To allow for independent variations of the inner and outer radii, we define the particle swelling ratio via the volume ratio of the swollen and collapsed particles:

$$\alpha = \left(\frac{v}{v_0} \right)^{1/3} = \left(\frac{\alpha_{\text{out}}^3 - \gamma^3 \alpha_{\text{in}}^3}{1 - \gamma^3} \right)^{1/3}, \quad (6)$$

where $\alpha_{\text{in}} \equiv a/a_0$ and $\alpha_{\text{out}} \equiv b/b_0$ are the inner and outer swelling ratios, respectively, and $\gamma \equiv a_0/b_0$ is the ratio of the collapsed inner and outer radii.

In a coarse-grained model, we describe swelling of microgels via the Flory-Rehner theory of polymer networks [64–66]. Combining mixing entropy, polymer-solvent interactions, and elastic free energy, the free energy of a microgel of swelling ratio α is

$$\beta F(\alpha) = N_m[(\alpha^3 - 1) \ln(1 - \alpha^{-3}) + \chi(1 - \alpha^{-3})] + \frac{3}{2} N_{\text{ch}}(\alpha^2 - \ln \alpha - 1), \quad (7)$$

where $\beta \equiv 1/(k_B T)$ at temperature T , N_{mon} and N_{ch} are the monomer and chain numbers of the particle, and χ is the Flory solvency parameter, associated with polymer-solvent interactions. When applying the Flory-Rehner theory, choosing the reference particle radius to be the collapsed radius is equivalent to choosing the reference polymer volume fraction to be the random close-packed volume fraction of monomers in the collapsed state [Eq. (5)]. Our choice is consistent with the experimental synthesis, in which cross linking occurs at temperatures sufficiently high that the particles when unstrained are in their collapsed states. Previous studies [61,67] that have successfully fit the Flory-Rehner theory to light scattering data for swelling of thermoresponsive microgels have determined that the volume phase transition can be accurately predicted only if the Flory solvency parameter is treated as a function

of temperature and the polymer volume fraction ϕ_p , following the form

$$\chi(T, \phi_p) = \frac{1}{2} - A \left(1 - \frac{\theta}{T} \right) + C \phi_p + D \phi_p^2, \quad (8)$$

where θ is the theta temperature and A , C , and D are fit parameters. pNIPAM microgels in room-temperature water are typically characterized by $\chi < 0.5$ [61,67].

Interactions between a pair of microgels of respective outer radii b_i and b_j are modeled via a Hertzian effective pair potential [68]

$$v_H(r_{ij}) = \begin{cases} \epsilon_{ij} \left(1 - \frac{r_{ij}}{b_i + b_j} \right)^{5/2}, & r_{ij} < b_i + b_j \\ 0, & r_{ij} \geq b_i + b_j, \end{cases} \quad (9)$$

where r_{ij} is the center-to-center separation of particles i and j . Overlapping configurations ($r_{ij} < b_i + b_j$) can be physically associated with faceting of otherwise spherical microgels. Neglecting any influence of the cavity on the interaction strength, the amplitude of the pair potential is given by [68]

$$\epsilon_{ij} = \frac{8}{15} \left(\frac{1 - \nu_i^2}{Y_i} + \frac{1 - \nu_j^2}{Y_j} \right)^{-1} (b_i + b_j)^2 (b_i b_j)^{1/2}, \quad (10)$$

depending on the gel elastic properties through Young's moduli Y_i and the Poisson ratios ν_i . Assuming equal Poisson ratios ν of all particles, we have

$$\epsilon_{ij} = \frac{8}{15} \frac{Y_i Y_j}{Y_i + Y_j} \frac{(b_i + b_j)^2}{1 - \nu^2} (b_i b_j)^{1/2}. \quad (11)$$

Scaling theory of polymer gels in good solvents [69] predicts that the bulk modulus scales linearly with temperature and cross-linker density: $Y \sim k_B T N_{\text{ch}} / (b^3 - a^3)$. Thus,

$$\beta \epsilon_{ij} = C \frac{N_{\text{ch}}}{b_i^3 - a_i^3 + b_j^3 - a_j^3} \frac{(b_i + b_j)^2}{1 - \nu^2} (b_i b_j)^{1/2}, \quad (12)$$

where the proportionality constant C is used to calibrate the model with experiment. The total internal energy associated with pair interactions is then given by

$$U = \sum_{i < j=1}^N v_H(r_{ij}), \quad (13)$$

where, for each pair in the sum, the appropriate amplitude must be taken from Eq. (12). Note that, according to the Hertz model, as the cavity of a hollow microgel collapses (a decreases), the Young's modulus decreases, i.e., the microgel becomes softer. Thus, the presence of a cavity promotes deswelling and faceting of hollow microgels with increasing concentration.

Two limitations of our model should be noted. First, the model does not explicitly distinguish between faceting and interpenetration of microgels, which would generally involve different pair energies. Second, the model neglects anisotropic deformation of microgels.

B. Simulation methods

Within the Open Source Physics Library [70], we implemented the standard Metropolis algorithm [71,72], accepting

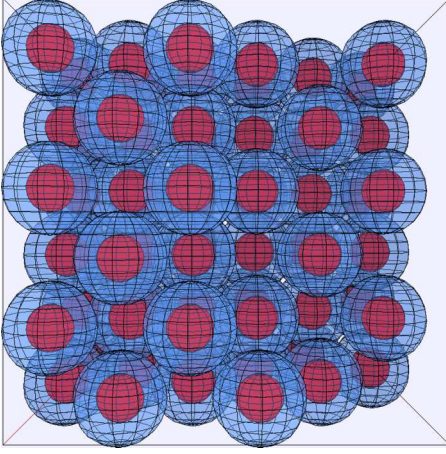


FIG. 14. Snapshot from a Monte Carlo simulation of a solution of soft, compressible, hollow microgels (blue spheres) with concentric cavities (red spheres).

a trial displacement and swelling ratio change ($\alpha \rightarrow \alpha'$) with probability

$$\mathcal{P}_{\text{acc}} = \min \{ \exp[-\beta(\Delta U + \Delta F)], 1 \}, \quad (14)$$

where ΔU is the change in internal energy [Eq. (13)] associated with interparticle (Hertz) pair interactions and $\Delta F = F(\alpha') - F(\alpha)$ is the change in free energy [Eq. (7)] associated with swelling. When moving a microgel, we *independently* made trial changes in both the inner and outer swelling ratios. As the particles moved and changed size and structure, we updated the Hertz potential amplitudes according to Eq. (12). After many trial moves, the particles adopt equilibrium size and configurational distributions that minimize the free energy.

To explore the dependence of microgel swelling and structure on concentration, we performed a series of simulations, each with $N = 256$ hollow microgels. For visualization, Fig. 14 depicts a typical snapshot from a smaller scale simulation of hollow microgels (blue spheres) with concentric spherical cavities (red spheres).

As input, the system parameters that can be varied are the average density, collapsed particle inner and outer radii, average cross-linker fraction, and Flory χ parameter. To model aqueous solutions of pNIPAM, we estimated $\chi \simeq 0.2$ from Eq. (8), using fit parameters from Ref. [61]. Although the synthesis yields microgels with a nominal cross-linker fraction of 5 mol%, the actual fraction, x , is likely much smaller. For purposes of illustration, we chose $x = 0.001$ but also examined smaller and larger values ($x = 0.0001, 0.01$). Since the collapsed radii are not known from experiments, we chose values for the inner (cavity) radius ($a_0 = 32$ nm or $a_0 = 50$ nm) and the outer radius ($b_0 = 63$ nm) that yield fully swollen inner and outer radii roughly consistent with experimental measurements of the hydrogenated hollow 5 mol% cross-linked microgels shown in Fig. 8 in the dilute limit: $a = 100$ nm and $b = 210$ nm, respectively. For the calibration factor in Eq. (12), we chose $C = 10$, corresponding to Young's moduli of order 10^3 kPa.

We initialized the simulations with microgels placed either on the sites of a perfect face-centered cubic (fcc) crystal

lattice or in a random configuration. The latter was generated by starting the particles on a lattice and running with pair interactions turned off for several thousand steps to allow the particles to randomize. Output data include the swollen microgel inner and outer radii, size polydispersity distributions, and the actual microgel volume fraction ϕ . We computed ϕ by summing the total volume occupied by the swollen particles (cavities included) and subtracting the pair intersection volumes. The densities considered here are sufficiently low that triplet intersections may be ignored. To assess phase stability, we computed bulk thermodynamic and structural properties, namely, the mean pair energy, osmotic pressure, radial distribution function, and static structure factor.

We computed the osmotic pressure from our simulations using the virial theorem, which relates the pressure

$$P = \frac{Nk_B T}{V} - \frac{1}{3V} \sum_{i < j=1}^N \langle r_{ij} v'_H(r_{ij}) \rangle \quad (15)$$

to the Hertz pair force, $-v'_H(r_{ij})$, exerted on microgel i by microgel j , where angular brackets denote an ensemble average over configurations in the canonical ensemble. From the particle coordinates, we computed the radial distribution function $g(r)$ by histogramming pair distances and the static structure factor via

$$S(q) = 1 + \frac{2}{N} \sum_{i < j=1}^N \left\langle \frac{\sin(qr_{ij})}{qr_{ij}} \right\rangle, \quad (16)$$

where q is the magnitude of the scattered wave vector.

C. Simulation results for single-particle properties of hollow microgels

First, we map ζ onto the actual volume fraction ϕ , which represents the real fraction of the volume occupied by the collapsed, deformed, and interpenetrated microgels. Figure 15 presents our simulation data for ϕ versus ζ . At very low concentrations ($\zeta \ll 1$), where interparticle interactions are weak, the microgels are barely compressed and $\phi \simeq \zeta$.

With increasing concentration, however, the data progressively deviate from the line $\phi = \zeta$, demonstrating both compression and faceting of the particles. For reference, Fig. 15 includes the horizontal line, $\phi = 0.7405$, which represents the maximum volume fraction of close-packed hard spheres. To exceed this limiting volume fraction, microgels must change shape, by either faceting or anisotropically deforming. With increasing ζ , the volume fraction of stiffer microgels ($x = 0.01$) plateaus just above the hard-sphere close-packed limit (blue squares in Fig. 15). In contrast, softer microgels ($x = 0.001$) both deswell and facet, as reflected by steady increase of ϕ (red empty circles). We verified that this trend continues as x is further lowered. These data show that the higher the cross-linker density, the stronger the tendency for microgels to deswell rather than facet in response to mutual crowding. Furthermore, enlarging the cavity from a collapsed inner radius of $a_0 = 32$ nm to $a_0 = 50$ nm results in a much more gradual increase of ϕ with increasing ζ (red solid circles).

The tendency for the volume fraction of hollow microgels with larger cavities to rise more gradually with increasing

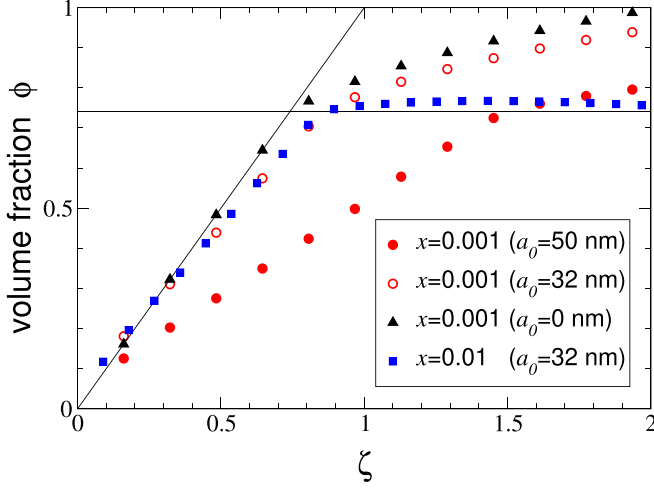


FIG. 15. Simulation data for actual volume fraction ϕ vs generalized volume fraction ζ in solutions of hollow microgels with collapsed outer radius $b_0 = 63$ nm, collapsed inner radius $a_0 = 32$ or 50 nm, Flory solvency parameter $\chi = 0.2$, and cross-linker fraction $x = 0.01$ or 0.001. The straight line, $\phi = \zeta$, represents incompressible microgels and the horizontal line, $\phi = 0.7405$, represents the close-packed limit for hard spheres. Data are shown also for softer, regular microgels with no cavity ($a_0 = 0$). Statistical error bars are smaller than symbols.

concentration is correlated with a weaker contraction of the cavity and stronger compression of the particles. These correlations are illustrated in Fig. 16, which shows that the mean outer radius progressively decreases with increasing ζ and a_0 , while the mean inner radius levels off when ϕ reaches close packing ($\zeta \simeq 1$ for $a_0 = 32$ nm and $\zeta \simeq 1.6$ for $a_0 = 50$ nm). (The probability distributions of inner and outer radii are presented in Fig. 22 of Appendix F.)

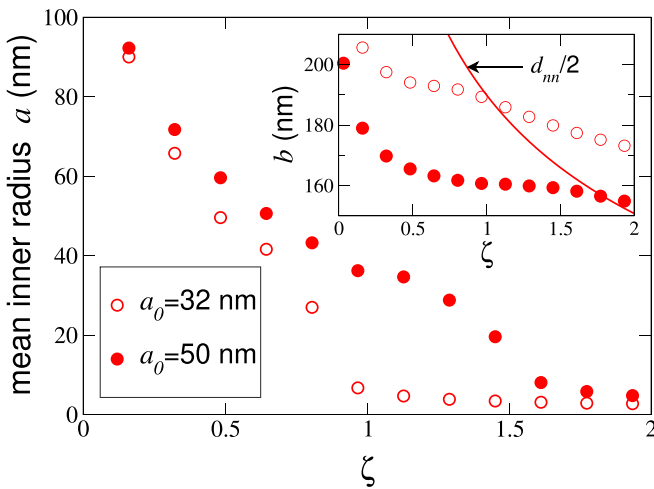


FIG. 16. Simulation data for mean swollen inner radius a and outer radius b (inset) vs generalized volume fraction ζ for systems of Fig. 15, with collapsed inner radius $a_0 = 32$ nm (empty circles) or 50 nm (solid circles), and cross-linker fraction $x = 0.001$. Statistical error bars are smaller than symbols. The curve is a fit of half the nearest-neighbor distance to the function $d_{nn}/2 = c\zeta^{-1/3}$ with fit parameter c for $a_0 = 32$ nm.

In the inset to Fig. 16, the curve is a fit of half the nearest neighbor distance for $a_0 = 32$ nm to the function $d_{nn}/2 = c\zeta^{-1/3}$, where $c = d_{nn}/2$ at $\zeta = 1$. Comparing with Fig. 13, we see qualitative consistency between simulation and SANS, in that the microgel diameter is smaller than the nearest neighbor distance ($2b < d_{nn}$) at lower concentrations, but crosses over and exceeds d_{nn} at higher concentrations. As ζ increases further, however, $2b > d_{nn}$ continues in the simulations, in contrast with the SANS data, which show another crossover. This discrepancy may be due to the neglect of anisotropic deformations of microgels in the simulation model.

The results in Fig. 15 show that regular microgels considerably deform (facet) for generalized volume fraction $\zeta > 0.75$, as reflected by the actual volume fraction exceeding the close-packed limit for hard spheres ($\phi \simeq 0.74$), while hollow microgels deform significantly less (i.e., ϕ is lower). This distinction is especially pronounced for the hollow microgels with the larger cavity ($a_0 = 50$ nm), for which faceting is predicted only for $\zeta > 1$. These observations further confirm our interpretation of the experimental data in Figs. 11 and 13: Hollow microgels are more compressible than regular microgels embedded in the same matrix of hollow microgels. It should be emphasized, however, that our simulation model does not distinguish between faceting and interpenetration of microgels.

D. Simulation results for bulk properties of hollow microgel solutions

To assess thermodynamic phase stability of hollow microgel solutions, we computed the osmotic pressure and mean pair energy versus concentration for systems initialized in either fcc crystal or random configurations (solid and empty symbols in Fig. 17, respectively). At lower ζ , the two branches of the equation of state (P vs ζ) and of the mean pair energy ($\langle U \rangle$ vs ζ) coincide, indicative of a fluid phase. At sufficiently high ζ , such that the volume fraction $\phi \simeq 0.5$ ($\zeta \simeq 0.55$ for $a_0 = 32$ nm and $\zeta \simeq 1$ for $a_0 = 50$ nm), the fcc branch splits off and drops below the random branch. This trend strongly suggests that, at a threshold concentration, which increases with increasing cavity size, the close-packed fcc crystal becomes stable and an amorphous solid metastable relative to the fluid. Interestingly, the pressure at the fluid-solid transition has a value that is nearly independent of cavity size and is about equal to that of a hard-sphere fluid [73]. While we have not computed free energies, which would require more extensive simulations for thermodynamic integrations, our results for the pressure and mean pair energy strongly support our interpretations.

To further support our conclusions regarding phase stability, we computed structural properties. Figure 18 shows the radial distribution function and static structure factor for hollow microgel solutions at concentrations ranging from just below to just above the fluid-solid transition. At lower ζ , the weak structure in $g(r)$ and $S(q)$ indicates a stable fluid phase. At higher ζ , systems initialized in an fcc crystal configuration remained in that structure, as reflected by distinct peaks in $g(r)$ and by a prominent main peak in $S(q)$ and distinct secondary peaks at higher q . In contrast, systems initialized in a random configuration remained amorphous, evidenced by a tall main

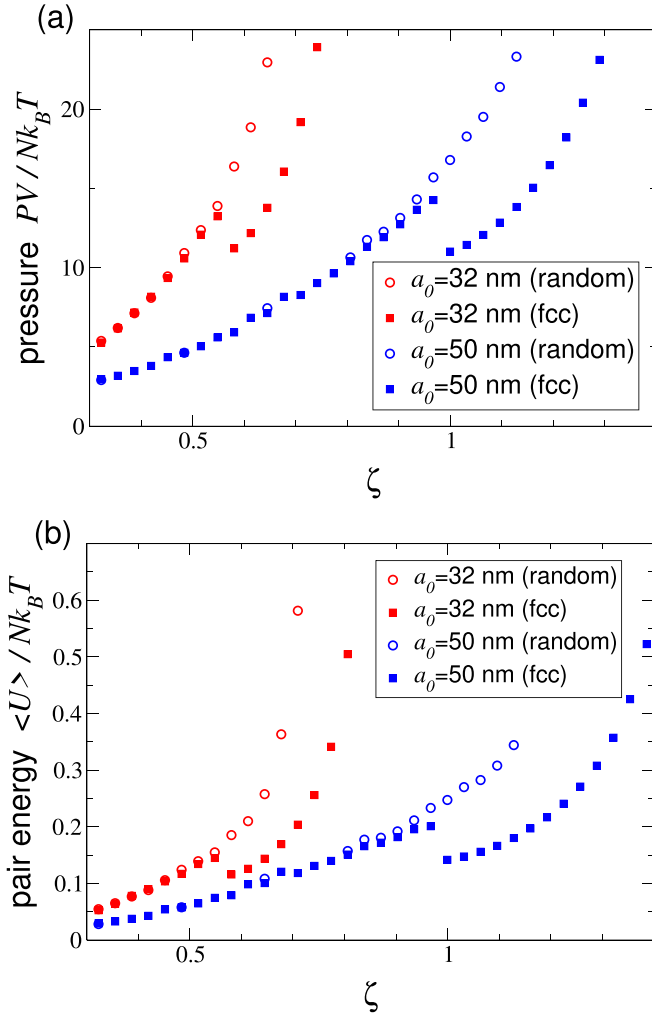


FIG. 17. Simulation data for bulk thermodynamic properties of hollow microgel solutions: (a) osmotic pressure P and (b) mean pair interaction energy $\langle U \rangle$ vs generalized volume fraction ζ in solutions with system parameters of Fig. 15, collapsed inner radius $a_0 = 32$ or 50 nm, and cross-linker fraction $x = 0.001$. Empty (solid) symbols represent data from runs initialized in random (fcc crystal) configurations. Statistical error bars are smaller than symbols.

peak in $S(q)$, but broad, shallow secondary peaks which are qualitatively similar to the $S(q)$ measured experimentally by SAXS and shown in Fig. 6.

Most importantly for interpreting experiments, larger cavity and lower cross-linker fraction are correlated with higher density up to which hollow microgels remain stable in the fluid phase. Our results illustrate the sensitive dependence of particle swelling and phase stability on cavity size, and the predicted trends support the absence of crystalline solids observed in experiments.

XI. CONCLUSIONS

To summarize, we presented results from experiments and simulations for the phase behavior of solutions of hollow microgels, soft colloidal particles composed of cross-linked polymeric networks swollen in a good solvent and distinguished by central, solvent-filled cavities. Crystals were not

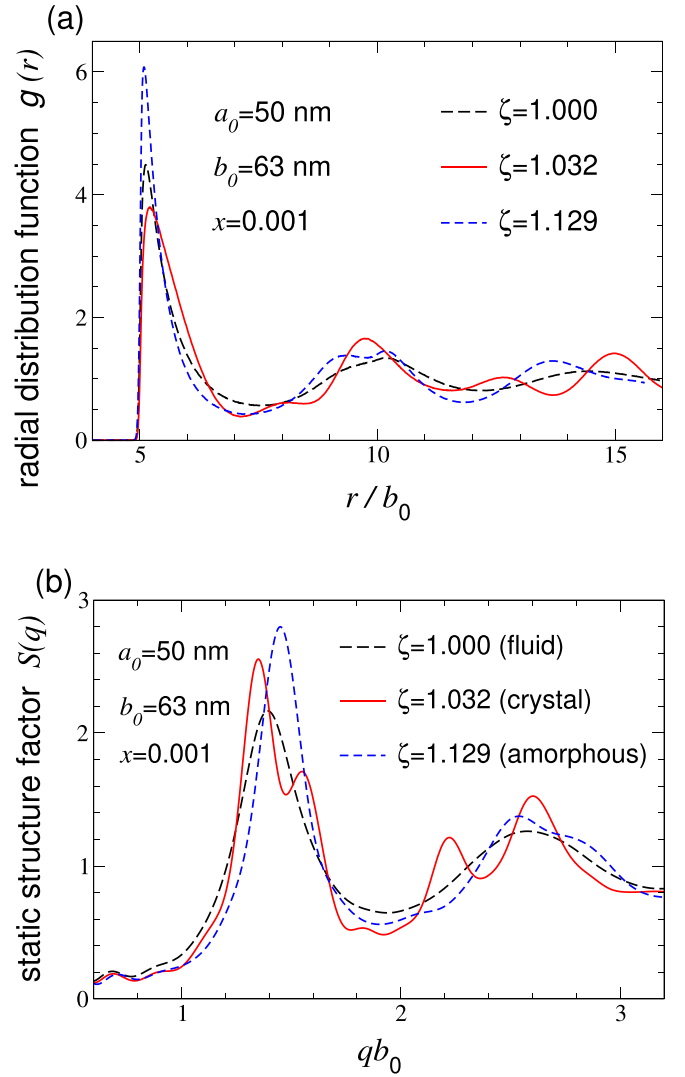


FIG. 18. Simulation data for bulk structural properties of hollow microgel solutions: (a) radial distribution function $g(r)$ vs radial distance r in units of collapsed microgel outer radius b_0 and (b) static structure factor $S(q)$ vs scattered wave vector q in solutions with system parameters of Fig. 15, collapsed inner radius $a_0 = 50$ nm, cross-link fraction $x = 0.001$, and generalized volume fractions ζ from fluid (black long-dashed curve) to solid phase, which may be either a fcc crystal (red solid curve) or amorphous (blue short-dashed curve).

observed, regardless of cavity size and amount of cross-linker agent used during synthesis. From SANS and SAXS measurements, we observed that at intermediate concentrations interpenetration between microgels is dominant. In contrast, at higher concentrations, in overcrowded conditions, the data indicate both faceting and anisotropic deformation of the microgels, in agreement with recent studies [8,22,37].

Monte Carlo simulations support our experimental findings on deswelling of hollow microgels and the inferences that cavities enhance stability of the fluid phase and are progressively occupied by polymer with increasing concentration. Our analyses of the bulk osmotic pressure, mean pair interaction energy, pair distribution function, and static structure factor

consistently indicate that a microgel solution freezes into either a close-packed crystal or an amorphous solid only when its *actual* volume fraction exceeds $\phi \simeq 0.5$, i.e., roughly the freezing density of a hard-sphere fluid. The key new insight from our modeling is that hollow microgels, because of their additional internal degrees of freedom, can delay the increase of ϕ with increasing generalized volume fraction by collapsing their cavities, and thus remain stable in the fluid phase up to considerably higher concentrations, ever more so for the larger cavities, consistent with experimental observations.

To rationalize the unique phase behavior of hollow microgels compared with that of both hard and soft spheres [74,75], the absence of a dense core must be considered. With increasing concentration, conventional colloids form crystals, the only way to increase their configurational entropy [76,77], as observed not only for hard-sphere-like systems (e.g., pMMA (poly(methylmethacrylate)) particles [1,78]), but also for regular microgels, core-polymer, and DNA-coated particles, which resemble hard spheres once the external soft shell is compressed and the dense, rigid core is reached [13,46–50].

In contrast, hollow microgels can deswell and deform with lower energetic cost due to fewer internal constraints. Furthermore, the polymer chains can rearrange within the empty cores. These two mechanisms offer an alternative pathway to increase configurational entropy without the need to crystallize. For sufficiently high concentrations, however, the collapsed chains may completely occupy the cavity. In this case, if the microgels are not jammed, crystals might form.

The absence of a crystalline phase for solutions of hollow microgels allows for studying glass formers or complex fluids without significant size disparities, making clear whether the unique properties of glasses, e.g., storage and loss moduli, depend on colloidal size disparities. Indeed, a general challenge to studying glass and jamming transitions of colloids is to avoid the formation of crystals in the system. A commonly used approach is to increase the size polydispersity of particles, e.g., by using binary mixtures [7]. However, this approach may face the risk of phase separation and crystallization of the two components in the mixture over a long period of time. Using solutions of hollow microgels overcomes this problem. Furthermore, it has been reported that relatively few hollow microgels embedded in a matrix of regular microgels of comparable size do not hinder crystallization [21]. Therefore, the role of hollow microgels as defects that suppress crystallization can be studied in binary mixtures of hollow and regular microgels. This study would open a path to a kind of defect that suppresses crystallization because of its internal structure, i.e., the absence of the core, and not because of a size mismatch, as is usually observed [1,74]. Finally, solutions of hollow microgels can be used to test some recent findings of simulations on the roles of deformation, interpenetration, and deswelling in the dynamics of soft colloids [79].

ACKNOWLEDGMENTS

Financial support from the Alexander von Humboldt Foundation, Deutsche Forschungsgemeinschaft within project A3 (Project No. 191948804) of the SFB 985 - Functional Microgels and Microgel Systems, and from the International

Helmholtz Research School of Biophysics and Soft Matter (IHRS BioSoft) is gratefully acknowledged. All SANS experiments were performed on D11 at the Institut Laue-Langevin (ILL), Grenoble, France. A.R.D. acknowledges support of the National Science Foundation (Grant No. DMR-1928073). Authors are thankful to Dr. A. Menzel and to the EUSMI program for the help with the measurements performed on the cSAXS beamline of the Swiss Light Source, Paul Scherrer Institut.

Data availability. All the data used for this study are available in Ref. [80].

APPENDIX A: PARTITION FUNCTION FOR HARD-SPHERE-LIKE SYSTEMS

As mentioned in the main text, hard-sphere-like systems crystallize because their positional ordering increases the configurational entropy, since the particles have more free space to jiggle around their equilibrium positions than in a disordered arrangement. Examples of hard-sphere-like particles suspended in a solvent include pMMA hard colloidal microspheres and colloids consisting of a more rigid core surrounded by a softer shell, such as microgels or DNA-coated silica particles. To demonstrate that the decrease in the Helmholtz free energy ($F = E - TS$) is purely driven by an increase in the entropy (S), and does not depend on a decrease of the internal energy (E), the partition function Z of the system must be considered,

$$Z = \frac{1}{h^{3N} N!} \int \cdots \int d\mathbf{p}^N d\mathbf{q}^N \exp[-\beta H(\mathbf{p}^N, \mathbf{q}^N)], \quad (\text{A1})$$

where $\beta = (k_B T)^{-1}$ and $H(\mathbf{p}^N, \mathbf{q}^N)$ is the Hamiltonian of the system, which is a function of the momenta \mathbf{p}^N and of the coordinates \mathbf{q}^N of the N hard spheres. The Hamiltonian can be decomposed into the sum of the kinetic energy of the system, $K(\mathbf{p}^N)$, and the potential energy, $U(\mathbf{q}^N)$. Colloidal dispersions of hard spheres (or hard-sphere-like particles) can be treated neglecting quantum mechanical effects and, therefore, the integration of Eq. (A1) can be performed over the momenta, leading to a term depending on T only: $(3/2)Nk_B T$. In this way, we can decouple the kinetic part of the Hamiltonian from the configurational part, Q :

$$Q = \frac{1}{N!} \int \cdots \int d\mathbf{q}^N \exp[-\beta U(\mathbf{q}^N)]. \quad (\text{A2})$$

Q is in general a function of N , T , and V , the total volume of the system. Now, if the particles interact with a hard-sphere pair potential, i.e., zero for distances exceeding the hard-sphere diameter and infinite elsewhere, we can write the average potential energy as

$$\langle U \rangle = -\frac{\partial \ln Q}{\partial \beta} = 0, \quad (\text{A3})$$

implying that the average energy for a system of hard-sphere-like particles equals only the average kinetic energy. Since the latter depends only on T , once T is fixed, E is constant. The only means of minimizing $F = E - TS$ is then to maximize the entropy S , which a hard-sphere-like system achieves by forming an ordered lattice. The loss in configurational energy is then overcome by the gain in entropy because of the

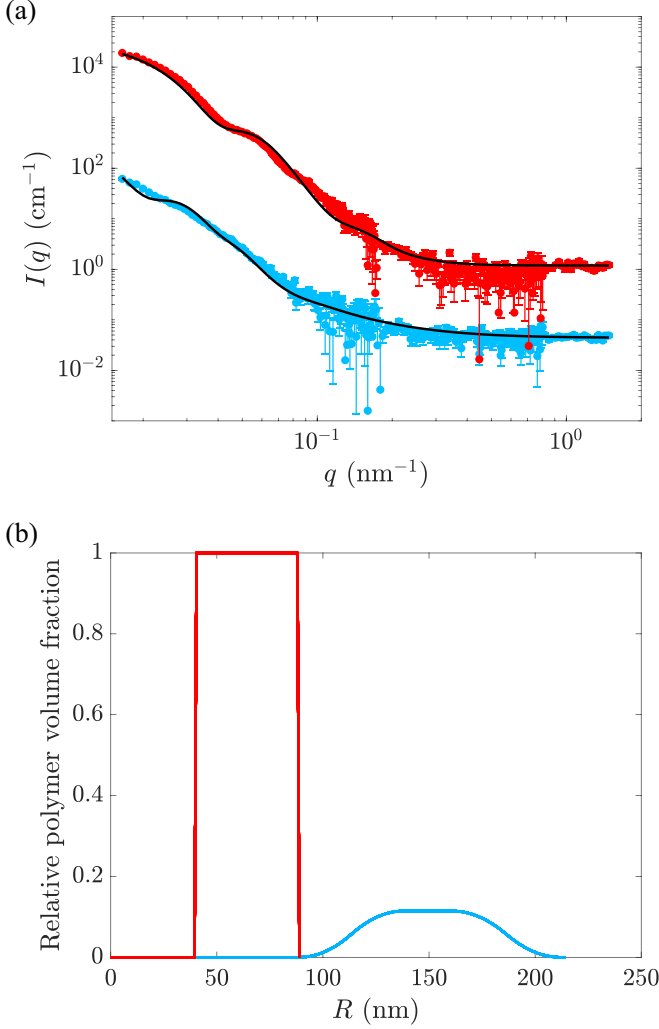


FIG. 19. (a) SANS intensities, $I(q)$, vs scattering vector, q , of deuterated hollow 5 mol% cross-linked microgels below (blue circles) and above (red circles) the VPTT, at 20 and 40 °C, respectively. The solid lines represent the fit of the data with the model in Ref. [23]. (b) Radial distributions of the relative polymer volume fraction as obtained by the fits of the curves in panel (a) using the model of Ref. [23]. The sample concentration is $\zeta = 0.081 \pm 0.005$.

increased space the hard spheres have to jiggle around their equilibrium positions [51,81]. The hollow microgels studied here, which are more easily deformable and possess an empty cavity in which the polymeric chains can rearrange upon increasing the generalized volume fraction of the solution, have

an alternative way to minimize the Helmholtz free energy—one that avoids long-range positional ordering.

APPENDIX B: FORM FACTOR OF THE DEUTERATED HOLLOW 5 MOL% CROSS-LINKED MICROGELS

As mentioned in the main text, for the SANS measurements with contrast variation, we needed to synthesize deuterated hollow 5 mol% cross-linked microgels. Figure 19 shows the form factors [Fig. 19(a)] and the resulting radial distributions of the relative polymer volume fraction within the microgel [Fig. 19(b)] as obtained by the fits of the curves in Fig. 19(a) using the model of Ref. [23] described in the main text. These samples were prepared in pure D_2O . As can be seen, the deuterated hollow 5 mol% cross-linked microgels maintain their cavity both below and above the volume phase transition temperature (VPTT), at 20 and 40 °C, respectively. The total radius is 212 ± 7 nm at 20 °C, while above the VPTT, the radius is 88 ± 5 nm. These particles are virtually identical to their hydrogenated counterpart.

APPENDIX C: RECAP OF THE CHARACTERISTIC LENGTHS OF THE MICROGELS DETERMINED BY SANS

In Table III, we report the characteristic lengths for the microgels used in this study. The results are obtained by fitting the SANS data relative to diluted suspensions of microgels measured below their VPTT, at 20.0 ± 0.01 °C. The MB-HS-60-5-pNIPAM and MB-HS-60-2.5-pNIPAM microgels were previously characterized in Ref. [21].

The reason that sample MB-HS-60-5-pNIPAM does not show internal fuzziness is that the internal interface of the cavity is, before the dissolution of the silica, connected to the rigid core. This can lead to different density within the polymeric network and consequent higher cross linking of the microgels in this region. Once the silica core is dissolved, the polymeric network maintains a different density and/or cross linking, which can hinder the internal fuzziness leading to the observed value $2\sigma_{\text{int}} = 0$. A similar behavior has been reported for similar hollow shell and hollow double-shell microgels [20,52].

APPENDIX D: STATIC LIGHT SCATTERING

Static light scattering data have been added to the data relative to dilute solution of the hydrogenated hollow 5 mol% cross-linked microgels studied by means of small-angle neutron scattering (SANS) with contrast variation to reach a lower q range. This addition cannot be done for the concentrated samples, since hydrogen and deuterium have the same

TABLE III. Characteristic lengths for the hollow and the regular microgels as obtained from the fit of the SANS data.

Sample name	R_{SANS} (nm)	p (%)	w_{core} (nm)	$2\sigma_{\text{int}}$ (nm)	w_s (nm)	$2\sigma_{\text{ext}}$ (nm)
MB-HS-105-5-D7pNIPAM	212 ± 7	15 ± 3	89 ± 2	49 ± 2	23 ± 2	51 ± 1
MB-HS-105-5-pNIPAM	210 ± 8	14 ± 1	91 ± 4	57 ± 2	10 ± 1	52 ± 1
MB-HS-60-5-pNIPAM	115 ± 3	8.9 ± 0.7	26 ± 1		14.8 ± 0.8	74.4 ± 0.9
MB-HS-60-2.5-pNIPAM	147 ± 4	7 ± 1	24 ± 2	34.6 ± 0.5	18.5 ± 0.3	69.9 ± 0.9
MB-pNIPAM-5-225	209 ± 4	13.2 ± 0.9			62 ± 1	147 ± 3

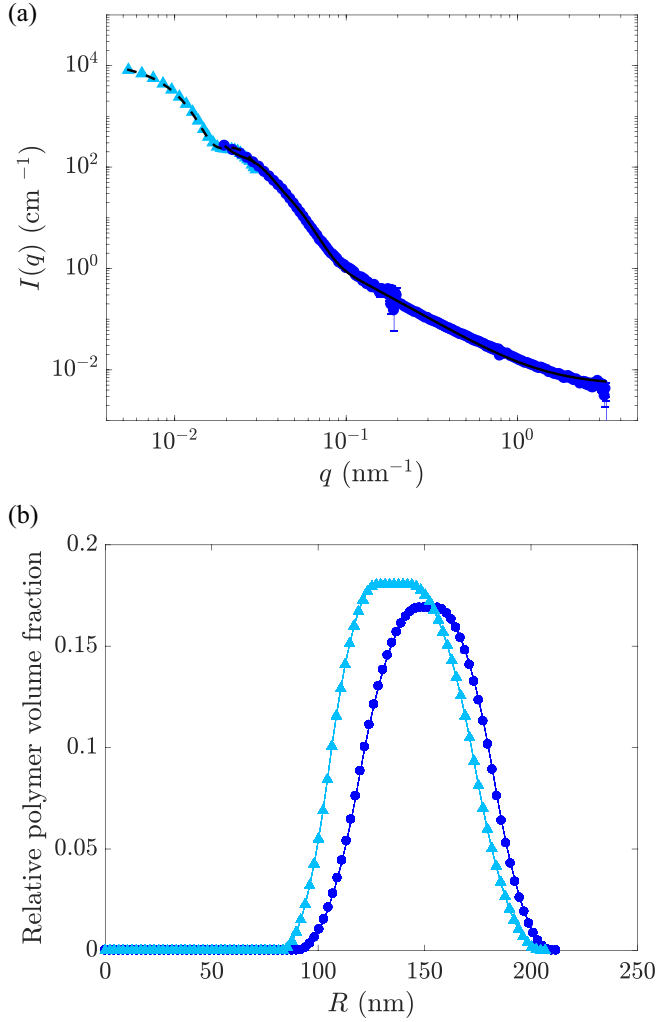


FIG. 20. (a) SANS (circles) and SLS (triangles) scattered intensities $I(q)$ of the hydrogenated hollow 5 mol% cross-linked microgels vs scattering vector q . The solid curves represent the data fits using the model in Ref. [23]. The sample had a $\zeta = 0.080 \pm 0.003$ and a temperature $T = 20.0 \pm 0.01$ °C. (b) Radial distribution of the relative polymer volume fraction within the microgel as obtained from the SANS and SLS data fit. Colors, symbols, and concentrations in panel (b) correspond to those in panel (a).

contrast in light scattering and the samples are not contrast matched.

To avoid the influence of microgel-microgel interactions on the form factor measurements in our static light scattering (SLS) experiments, we worked with highly diluted samples, for which the structure factor, $S(q)$, can be approximated to unity and $I(q) \approx P(q)$, with $I(q)$ and $P(q)$ being the total scattered intensity and the form factor, respectively. A closed goniometer from SLS-Systemtechnik GmbH, mounting a laser with a wavelength in vacuum of $\lambda_0 = 640$ nm, was used for all measurements. The instrument covers a q range lower than that of small-angle neutron and x-ray scattering and therefore complements these methods. An index-matched toluene bath was used to keep the temperature constant during the measurements. The scattering angle, θ , was varied between 15° and 150° , thereby varying the wave vector $q = (4\pi n/\lambda_0) \sin(\theta/2)$. All measurements were corrected by sub-

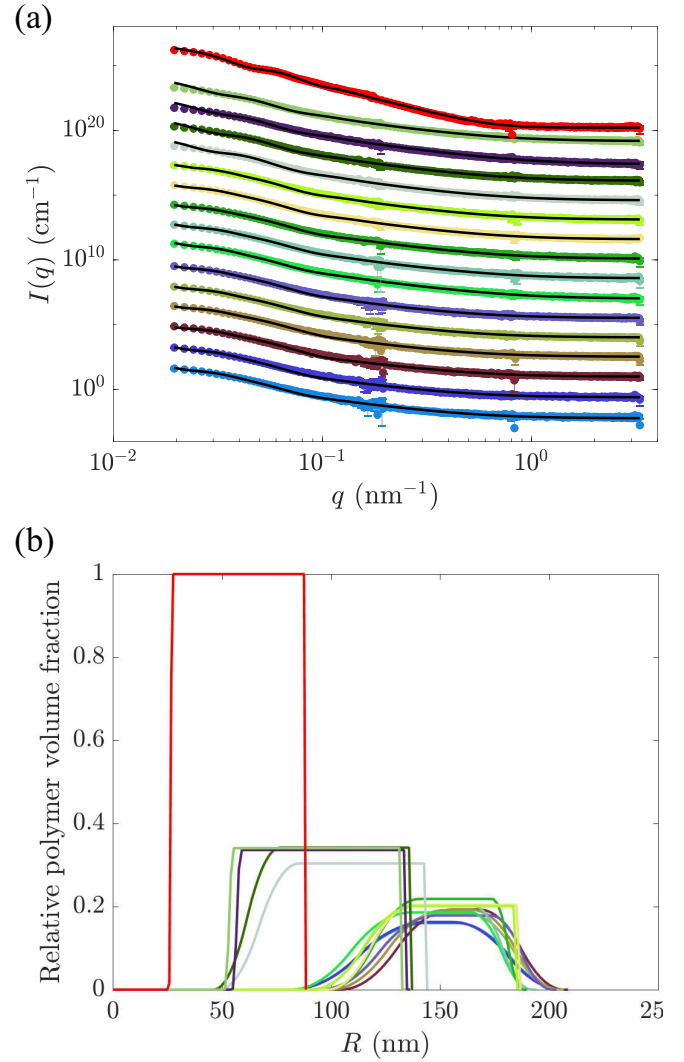


FIG. 21. (a) Additional SANS intensities, $I(q)$, vs scattering vector, q , of hydrogenated hollow 5 mol% cross-linked microgels. (b) Radial distribution of the relative polymer volume fraction as obtained by fitting the curves in panel (a) using the model of Ref. [23]. In panel (a), the concentrations from bottom to top are $\zeta = 0.20 \pm 0.01$, 0.25 ± 0.01 , 0.35 ± 0.01 , 0.40 ± 0.01 , 0.45 ± 0.01 , 0.50 ± 0.01 , 0.55 ± 0.01 , 0.60 ± 0.01 , 0.70 ± 0.01 , 0.74 ± 0.01 , 0.76 ± 0.02 , 0.90 ± 0.02 , 0.95 ± 0.02 , 1.00 ± 0.02 , 1.10 ± 0.02 , and $\zeta < 0.080 \pm 0.003$. The top curve is at $T = 40.0 \pm 0.1$ °C, while all the other measurements are at $T = 20.0 \pm 0.1$ °C. In panel (b), the colors and therefore the concentrations correspond to the colors in panel (a).

tracting the dark count and the scattered intensity of the solvent and the cell.

Figure 20(a) shows the scattered intensities obtained from SANS (circles) and SLS (triangles) of the hydrogenated hollow 5 mol% cross-linked microgels at $\zeta = 0.08 \pm 0.01$ combined together. The radial distribution of the relative polymer volume fractions within the microgels are reported in Fig. 20(b). Both methods confirm the presence of the internal cavity. The difference in the radial profiles may be due to the different sensitivities of neutron and light to the dangling chains in the inner and outer peripheries of the hollow microgels.

APPENDIX E: ADDITIONAL SANS DATA AND FITS

Above the VPTT, the hydrogenated hollow 5 mol% cross-linked microgels collapse to 88 ± 2 nm and no fuzziness is detected (red curves in Fig. 21). The internal cavity shrinks with respect to the swollen state to a radius of 25.9 ± 0.8 nm, as already reported both from SANS experiments and molecular dynamics simulations [20,22,23,52,59].

The other curves in Fig. 21 are the SANS form factors of the hydrogenated hollow 5 mol% cross-linked microgels measured with the tracing method at different concentrations [Fig. 21(a)] and the radial distributions of the relative polymer volume fraction within the microgels as obtained by fitting the data with the fuzzy-shell core model (b). All the curves in Fig. 21 are measured at 20 °C, except for the red curves, which were measured at 40 °C.

In performing the fits, we fixed the value of the volume fraction of w_s (Fig. 7) to 1. The data were then normalized to the area under the radial distribution of the collapsed state, since (i) above the VPTT the microgels have a more defined profile with higher contrast due to the collapsed polymer and (ii) the mass of the polymer is conserved. The graphs in Fig. 21(b) show that in the swollen state the polymer occupies ≈ 40 and 20% of the volume occupied in the collapsed state. As reported by Dubbert *et al.* [20], as well as more recently by Schmid *et al.* [52], SANS shows that the polymer volume fraction within a microgel well above the VPTT is $\approx 75\%$. This property can be considered valid also for our microgels, since they have been synthesised with similar protocols and are based on pNIPAM as well. Thus, in the swollen state the volume fraction of polymer in the core is $\approx 20\%$. Also, this value agrees with the values reported in the literature [20,52].

APPENDIX F: ADDITIONAL SIMULATION RESULTS

Figure 22 shows our simulation results for the probability distributions of the inner and outer swelling ratios of hollow microgels, obtained by histogramming the inner and outer microgel radii. With increasing concentration, the particles exhibit progressive deswelling and cavity collapse, consistent with Fig. 16 and with the SANS measurements of radial distributions of relative polymer volume fraction (Fig. 8).

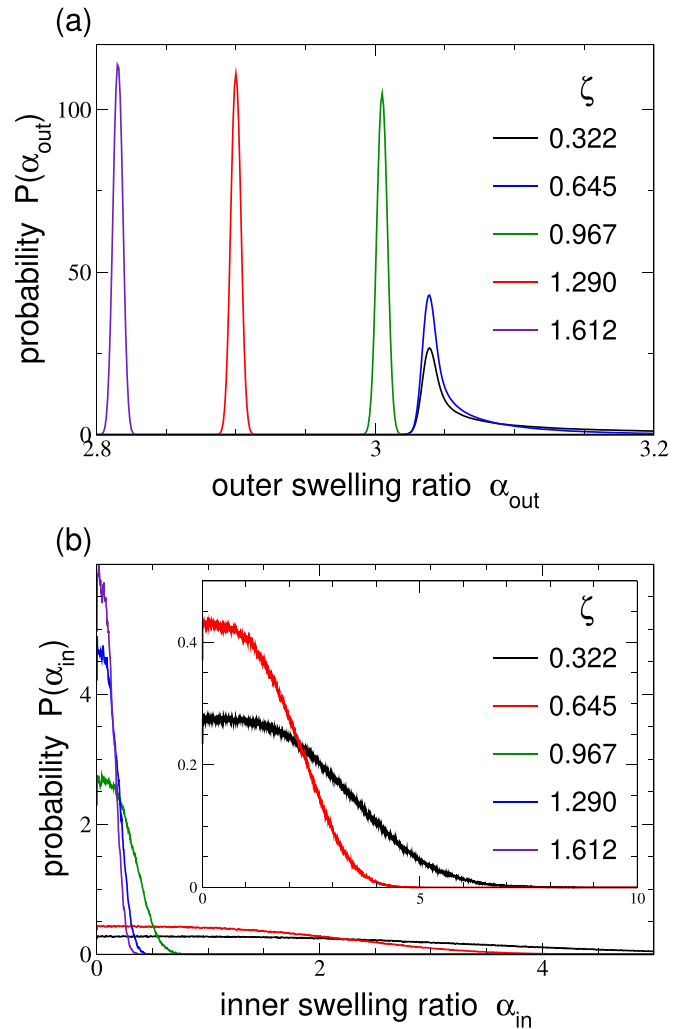


FIG. 22. Probability distributions of outer (a) and inner (b) swelling ratios of hollow microgels in solution with system parameters of Fig. 15, collapsed inner radius $a_0 = 32$ nm, cross-link fraction $x = 0.001$, and generalized volume fraction ζ increasing from right to left as shown. Inset to panel (b) shows distributions for lowest ζ values on a larger scale.

- [1] P. N. Pusey and W. van Megen, *Nature (London)* **320**, 340 (1986).
- [2] J. M. Kim, J. Fang, A. P. R. Eberle, R. Castaneda-Priego, and N. J. Wagner, *Phys. Rev. Lett.* **110**, 208302 (2013).
- [3] D. Rosenbaum, P. C. Zamora, and C. F. Zukoski, *Phys. Rev. Lett.* **76**, 150 (1996).
- [4] U. Gasser, E. R. Weeks, A. Schofield, P. N. Pusey, and D. A. Weitz, *Science* **292**, 2580 (2001).
- [5] M. Stieger, J. S. Pedersen, P. Lindner, and W. Richtering, *Langmuir* **20**, 7283 (2004).
- [6] A. S. J. Iyer and L. A. Lyon, *Angew. Chem. Int. Ed.* **48**, 4562 (2009).
- [7] J. Mattsson, H. M. Wyss, A. Fernandez-Nieves, K. Miyazaki, Z. Hu, D. R. Reichman, and D. A. Weitz, *Nature (London)* **462**, 83 (2009).
- [8] P. van der Scheer, T. van de Laar, J. van der Gucht, D. Vlassopoulos, and J. Sprakel, *ACS Nano* **11**, 6755 (2017).
- [9] X. Ma, Z. S. Davidson, T. Still, R. J. S. Ivancic, S. S. Schoenholz, A. J. Liu, and A. G. Yodh, *Phys. Rev. Lett.* **122**, 028001 (2019).
- [10] H. Senff and W. Richtering, *J. Chem. Phys.* **111**, 1705 (1999).
- [11] A. M. Alsayed, M. F. Islam, J. Zhang, P. J. Collings, and A. G. Yodh, *Science* **309**, 1207 (2005).
- [12] M. Pelaez-Fernandez, A. Souslov, L. A. Lyon, P. M. Goldbart, and A. Fernandez-Nieves, *Phys. Rev. Lett.* **114**, 098303 (2015).
- [13] A. Scotti, U. Gasser, E. S. Herman, J. Han, A. Menzel, L. A. Lyon, and A. Fernandez-Nieves, *Phys. Rev. E* **96**, 032609 (2017).
- [14] Y. Han, N. Y. Ha, A. M. Alsayed, and A. G. Yodh, *Phys. Rev. E* **77**, 041406 (2008).

- [15] M. Rey, M. A. Fernandez-Rodriguez, M. Steinacher, L. Scheidegger, K. Geisel, W. Richtering, T. M. Squires, and L. Isa, *Soft Matter* **12**, 3545 (2016).
- [16] Y. Peng, W. Li, F. Wang, T. Still, A. G. Yodh, and Y. Han, *Nat. Commun.* **8**, 14978 (2017).
- [17] Z. Zhang, N. Xu, D. T. N. Chen, P. Yunker, A. M. Alsayed, K. B. Aptowicz, P. Habdas, S. R. N. A. J. Liu, and A. G. Yodh, *Nature (London)* **459**, 230 (2009).
- [18] D. Paloli, P. S. Mohanty, J. J. Crassous, E. Zaccarelli, and P. Schurtenberger, *Soft Matter* **9**, 2927 (2013).
- [19] S. Nayak, D. Gan, M. Serpe, and L. Lyon, *Small* **1**, 416 (2005).
- [20] J. Dubbert, T. Honold, J. S. Pedersen, A. Radulescu, M. Drechsler, M. Karg, and W. Richtering, *Macromolecules* **47**, 8700 (2014).
- [21] A. Scotti, A. R. Denton, M. Brugnioni, J. E. Houston, R. Schweins, I. I. Potemkin, and W. Richtering, *Macromolecules* **52**, 3995 (2019).
- [22] A. Scotti, M. Brugnioni, A. A. Rudov, J. E. Houston, I. I. Potemkin, and W. Richtering, *J. Chem. Phys.* **148**, 174903 (2018).
- [23] J. Dubbert, K. Nothdurft, M. Karg, and W. Richtering, *Macromol. Rapid Commun.* **36**, 159 (2015).
- [24] W. Stöber, A. Fink, and E. Bohn, *J. Colloid Interface Sci.* **26**, 62 (1968).
- [25] L. Zha, Y. Zhang, W. Yang, and S. Fu, *Adv. Mater.* **14**, 1090 (2002).
- [26] A. Scotti, W. Liu, J. S. Hyatt, E. S. Herman, H. S. Choi, J. Kim, L. A. Lyon, U. Gasser, and A. Fernandez-Nieves, *J. Chem. Phys.* **142**, 234905 (2015).
- [27] D. E. Koppel, *J. Chem. Phys.* **57**, 4814 (1972).
- [28] W. Burchard and W. Richtering, *Progr. Colloid Polym. Sci.* **80**, 151 (1989).
- [29] H. Shirota and K. Horie, *Chem. Phys.* **242**, 115 (1999).
- [30] M. Brugnioni, A. C. Nickel, L. C. Kröger, A. Scotti, A. Pich, K. Leonhard, and W. Richtering, *Polym. Chem.* **10**, 2397 (2019).
- [31] S. W. Provencher, *Comput. Phys. Commun.* **27**, 213 (1982).
- [32] I. Bouhid de Aguiar, T. van de Laar, M. Meireles, A. Bouchoux, J. Sprakel, and K. Schreën, *Sci. Rep.* **7**, 10223 (2017).
- [33] G. M. Conley, P. Aebischer, S. Nöjd, P. Schurtenberger, and F. Scheffold, *Sci. Adv.* **3**, e1700969 (2017).
- [34] A. Scotti, M. Pelaez-Fernandez, U. Gasser, and A. Fernandez-Nieves, *Phys. Rev. E* **103**, 012609 (2021).
- [35] A. Scotti, U. Gasser, E. S. Herman, M. Pelaez-Fernandez, L. A. Lyon, and A. Fernandez-Nieves, *Proc. Natl. Acad. Sci. USA* **113**, 5576 (2016).
- [36] P. S. Mohanty, S. Nöjd, K. v. Gruijthuijsen, J. J. Crassous, M. Obiols-Rabasa, R. Schweins, A. Stradner, and P. Schurtenberger, *Sci. Rep.* **7**, 1487 (2017).
- [37] G. M. Conley, C. Zhang, P. Aebischer, J. L. Harden, and F. Scheffold, *Nat. Commun.* **10**, 2436 (2019).
- [38] U. Gasser, *J. Phys.: Condens. Matter* **21**, 203101 (2009).
- [39] A. Scotti, J. E. Houston, M. Brugnioni, M. M. Schmidt, M. F. Schulte, S. Bochenek, R. Schweins, A. Feoktystov, A. Radulescu, and W. Richtering, *Phys. Rev. E* **102**, 052602 (2020).
- [40] U. Gasser, A. Scotti, and A. Fernandez-Nieves, *Phys. Rev. E* **99**, 042602 (2019).
- [41] J. Brijitta, B. Tata, R. Joshi, and T. Kaliyappan, *J. Chem. Phys.* **131**, 074904 (2009).
- [42] A. N. St. John, V. Breedveld, and L. A. Lyon, *J. Phys. Chem. B* **111**, 7796 (2007).
- [43] L. A. Lyon, J. D. Debord, S. B. Debord, C. D. Jones, J. G. McGrath, and M. J. Serpe, *J. Phys. Chem. B* **108**, 19099 (2004).
- [44] J. D. Debord, S. Eustis, S. Byul Debord, M. T. Lofye, and L. A. Lyon, *Adv. Mat.* **14**, 658 (2002).
- [45] S. B. Debord and L. A. Lyon, *J. Phys. Chem. B* **107**, 2927 (2003).
- [46] A. Scotti, S. Bochenek, M. Brugnioni, M. A. Fernandez-Rodriguez, M. F. Schulte, J. E. Houston, A. P. H. Gelissen, I. I. Potemkin, L. Isa, and W. Richtering, *Nat. Commun.* **10**, 1418 (2019).
- [47] J. J. Crassous, M. Siebenbürger, M. Ballauff, M. Drechsler, O. Henrich, and M. Fuchs, *J. Chem. Phys.* **125**, 204906 (2006).
- [48] J. J. Crassous, A. Wittemann, M. Siebenbürger, M. Schrunner, M. Drechsler, and M. Ballauff, *Colloid Polym. Sci.* **286**, 805 (2008).
- [49] W. Cheng, M. R. Hartman, D.-M. Smilgies, R. Long, M. J. Campolongo, R. Li, K. Sekar, C.-Y. Hui, and D. Luo, *Angew. Chem. Int. Ed.* **49**, 380 (2010).
- [50] J. Zhang, P. M. Lettinga, J. K. G. Dhont, and E. Stiakakis, *Phys. Rev. Lett.* **113**, 268303 (2014).
- [51] M. Baus, *J. Stat. Phys.* **48**, 1129 (1987).
- [52] A. J. Schmid, J. Dubbert, A. A. Rudov, J. S. Pedersen, P. Lindner, M. Karg, I. I. Potemkin, and W. Richtering, *Sci. Rep.* **6**, 22736 (2016).
- [53] D. Frenkel, *Nature (London)* **460**, 465 (2009).
- [54] U. Gasser, J.-J. Liotor-Santos, A. Scotti, O. Bunk, A. Menzel, and A. Fernandez-Nieves, *Phys. Rev. E* **88**, 052308 (2013).
- [55] U. Gasser, J. S. Hyatt, J.-J. Liotor-Santos, E. S. Herman, L. A. Lyon, and A. Fernandez-Nieves, *J. Chem. Phys.* **141**, 034901 (2014).
- [56] J. Liu, H.-J. Schöpe, and T. Palberg, *Part. Part. Syst. Charact.* **17**, 206 (2000).
- [57] V. F. Seras, *Neutron News* **3** (1992).
- [58] I. Berndt, J. S. Pedersen, and W. Richtering, *Angew. Chem. Int. Ed.* **45**, 1737 (2006).
- [59] M. Brugnioni, A. Scotti, A. A. Rudov, A. P. H. Gelissen, T. Caumanns, A. Radulescu, T. Eckert, A. Pich, I. I. Potemkin, and W. Richtering, *Macromolecules* **51**, 2662 (2018).
- [60] M. Stieger, W. Richtering, J. Pedersen, and P. Lindner, *J. Chem. Phys.* **120**, 6197 (2004).
- [61] A. Fernandez-Barbero, A. Fernandez-Nieves, I. Grillo, and E. Lopez-Cabarcos, *Phys. Rev. E* **66**, 051803 (2002).
- [62] J. S. Pedersen, D. Posselt, and K. Mortensen, *J. Appl. Crystallogr.* **23**, 321 (1990).
- [63] F. Scheffold and T. Mason, *J. Phys.: Condens. Matter* **21**, 332102 (2009).
- [64] P. J. Flory, *Principles of Polymer Chemistry* (Cornell University Press, Ithaca, NY, 1953).
- [65] P. J. Flory and J. Rehner, *J. Chem. Phys.* **11**, 512 (1943).
- [66] P. J. Flory and J. Rehner, *J. Chem. Phys.* **11**, 521 (1943).
- [67] C. G. Lopez and W. Richtering, *Soft Matter* **13**, 8271 (2017).
- [68] L. D. Landau and E. M. Lifshitz, *Theory of Elasticity*, 3rd ed. (Elsevier, Amsterdam, 1986).
- [69] P.-G. de Gennes, *Scaling Concepts in Polymer Physics* (Cornell University Press, Ithaca, NY, 1979).
- [70] H. Gould, J. Tobochnik, and W. Christian, *Introduction to Computer Simulation Methods* (Addison Wesley, Reading, MA, 2006).

- [71] D. Frenkel and B. Smit, *Understanding Molecular Simulation*, 2nd ed. (Academic Press, London, 2001).
- [72] K. Binder and D. W. Heermann, *Monte Carlo Simulation in Statistical Physics: An Introduction*, 5th ed. (Springer, Berlin, 2010).
- [73] J.-P. Hansen and I. R. McDonald, *Theory of Simple Liquids*, 3rd ed. (Elsevier, London, 2006).
- [74] S. Auer and D. Frenkel, *Nature (London)* **409**, 1020 (2001).
- [75] J. C. Pàmies, A. Cacciuto, and D. Frenkel, *J. Chem. Phys.* **131**, 044514 (2009).
- [76] D. Frenkel, *J. Phys.: Condens. Matter* **6**, A71 (1994).
- [77] D. Frenkel, *Phys. A (Amsterdam, Neth.)* **263**, 26 (1999).
- [78] P. Pusey, *J. Phys.* **48**, 709 (1987).
- [79] N. Gnan and E. Zaccarelli, *Nat. Phys.* **15**, 683 (2019).
- [80] All the data used for this study are available by request at <https://hdl.handle.net/21.11102/74326e3e-1b59-11ea-9a63-e41f1366df48>. SANS data are available at DOI: [10.5291/ILL-DATA.9-11-1855](https://doi.org/10.5291/ILL-DATA.9-11-1855).
- [81] H. Löwen, in *Statistical Physics and Spatial Statistics* (Springer, Berlin, 2000), pp. 295–331.